THE CORTICAL WIRING SCHEME OF HIERARCHICAL INFORMATION PROCESSING

Casey Paquola[1*], Jakob Seidlitz[2,3], Oualid Benkarim[1], Jessica Royer[1], Petr Klimes[4], Richard A. I. Bethlehem[3], Sara Lariviere[1], Reinder Vos de Wael[1], Jeffery A. Hall[4], Birgit Frauscher[4], Jonathan Smallwood[5], Boris C. Bernhardt[1*]

[1] Multimodal Imaging and Connectome Analysis Lab, McConnell Brain Imaging Centre, Montreal Neurological Institute and Hospital, McGill University, Montreal, Quebec, Canada; [2] Developmental Neurogenomics Unit, National Institute of Mental Health, Bethesda, MD, USA; [3] Department of Psychiatry, University of Cambridge, Cambridge, United Kingdom; [4] Montreal Neurological Institute and Hospital, McGill University, Montreal, Quebec, Canada; [5] York Neuroimaging Center, University of York, York, United Kingdom

* Correspondence to casey.paquola@mail.mcgill.ca or boris.bernhardt@mcgill.ca

ABSTRACT

The vast net of fibres within and underneath the cortical mantle is optimised to support the convergence of different levels of brain organisation, specifically through linking cellular and architectural features of different cortical areas to give rise to more integrated neural function. Leveraging multimodal neuroimaging and machine learning techniques, we identified a novel manifold space that is governed by geometric, microstructural, and connectional aspects of cortico-cortical wiring. Principal dimensions of this manifold recapitulated established sensory-limbic and anterior-posterior gradients of brain organisation, and were found to reflect neural and glial gradients of cytoarchitectural organisation and gene expression. Manifold features were accurate in predicting cortico-cortical functional interactions derived from resting-state functional neuroimaging. Furthermore, application of this approach to a group of neurological patients, who underwent intracerebral encephalographic recordings, established that manifold features also explained the direction of information flow between different cortical areas. These results advance our understanding of how cell-specific neurobiological gradients produce a hierarchical cortical wiring scheme that is concordant with increasing functional sophistication of human brain organisation.

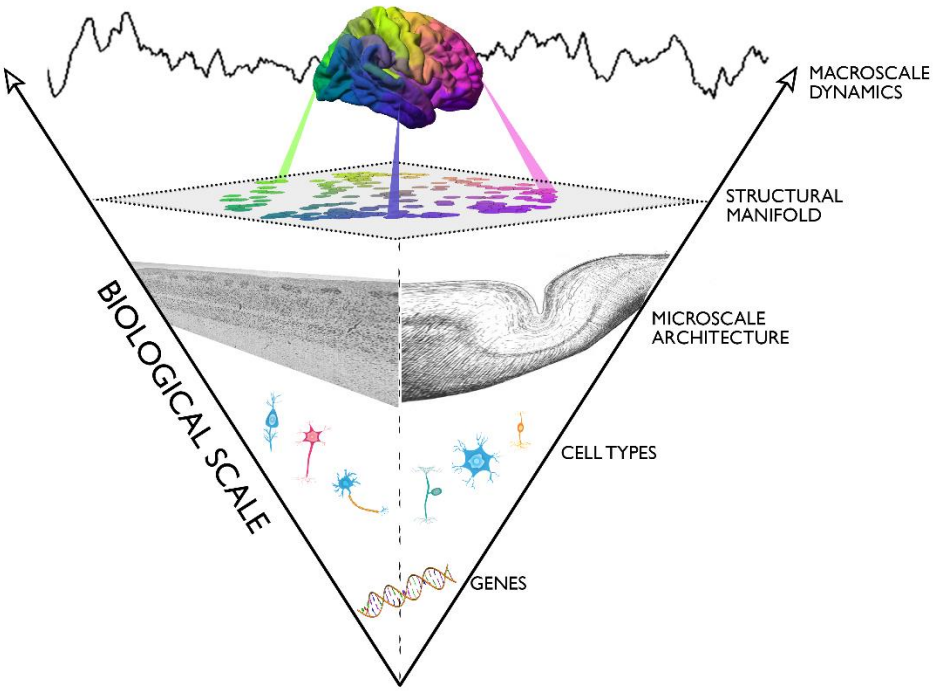

INTRODUCTION

Cortical neuronal activity is simultaneously constrained by both local columnar circuitry and large-scale networks[1,2]. It is generally assumed that this interaction emerges because individual neurons are embedded in a global context through an intricate web of short- and long-range fibres. Developing a better model of this cortical wiring scheme is a key goal of systems neuroscience, because it would serve as a blueprint for the mechanisms through which local influences on neural function impact on spatially distant sites, and vice versa.

Post mortem histological and gene expression studies provide gold standard descriptions of how neurobiological and microstructural features are distributed across the cortex[3–6]. Histological and genetic properties of the brain often vary gradually together, mirroring known functional topographies and processing hierarchies[7]. This suggests that observed brain organisation may be the consequence of a set of consistent principles that are expressed across multiple scales (gene expression, cytoarchitecture, cortical wiring and macroscale function). Critically, full appreciation of how local and global features of brain organisation constrain neural function requires that multiple levels of brain organisation are mapped *in vivo*. To achieve this goal, our study capitalised on state-of-the-art magnetic resonance imaging (MRI) methods and machine learning techniques to build a novel model of the human cortical wiring scheme. We tested whether this model provides a meaningful description of how structure shapes macroscale brain function and the information flow between different systems. In particular, if our model successfully bridges the gap between micro- and macroscopic scales of neural organisation then it should describe local features of both cortical microcircuitry and its macroscale organisation, and deliver meaningful predictions for brain function. To this end, we established the neurobiological validity of the structural manifold by cross-referencing our newly developed model against *post mortem* histology and RNA sequencing data[5,8,9]. Finally, we assessed the utility of our model to understand macroscale features of brain function and information flow by assessing how well the model predicts resting-state connectivity obtained from functional MRI as well as directed descriptions of neural function provided by intracerebral stereo-electroencephalography.

Currently, the prevailing technique to infer structural connectivity in living humans is diffusion MRI tractography[10,11]. By approximating white matter fibre tracts *in vivo*[10–12], tractography has advanced our understanding of structural networks in health[13–15], disease[16–18], and shaped our understanding of the constraining role of brain structure on function[19–24]. Diffusion MRI tractography, however, has recognised limitations[25,26]. Crucially, the technique does not explicitly model intracortical axon collaterals and superficial white matter fibres, short-range fibres contributing to >90% of all cortico-cortical connections[27]. To address this gap, our approach combines diffusion tractography with two complementary facets of cortical wiring, namely spatial proximity and microstructural similarity. Spatial proximity predicts short cortico-cortical fibres[28,29], which transmit the most common type of neural information also referred to as "nearest-neighbour-or-next-door-but-one"[30]. Microstructural similarity also serves as a powerful predictor of inter-regional connectivity in non-human animals[31], whereby the "structural model" of cortico-cortical connectivity postulates that connectivity likelihood between two regions is primarily governed by their similarity in cytoarchitecture[32–35]. We recently developed and histologically validated microstructure profile covariance analysis, which quantifies microstructural similarity between different cortical areas *in vivo* through a systematic comparison of intracortical myelin sensitive neuroimaging profiles[7].

Together our study harnessed complementary *in vivo* features of structural connectivity to generate a blueprint of the human cortical wiring scheme. We hypothesised that this new structural manifold would have features that help understand both the neurobiological underpinnings of cortico-cortical functional differentiation and the manner with which this is distributed across the cortex[36,37].

RESULTS

A multi-scale model of cortical wiring

The wiring model was first derived from a *Discovery* subset of the Human Connectome Project dataset (n=100 unrelated adults) that offers high resolution structural magnetic resonance imaging (MRI), diffusion MRI, and microstructurally sensitive T1w/T2w maps[38] (**Figure 1A**, see *Methods* for details).

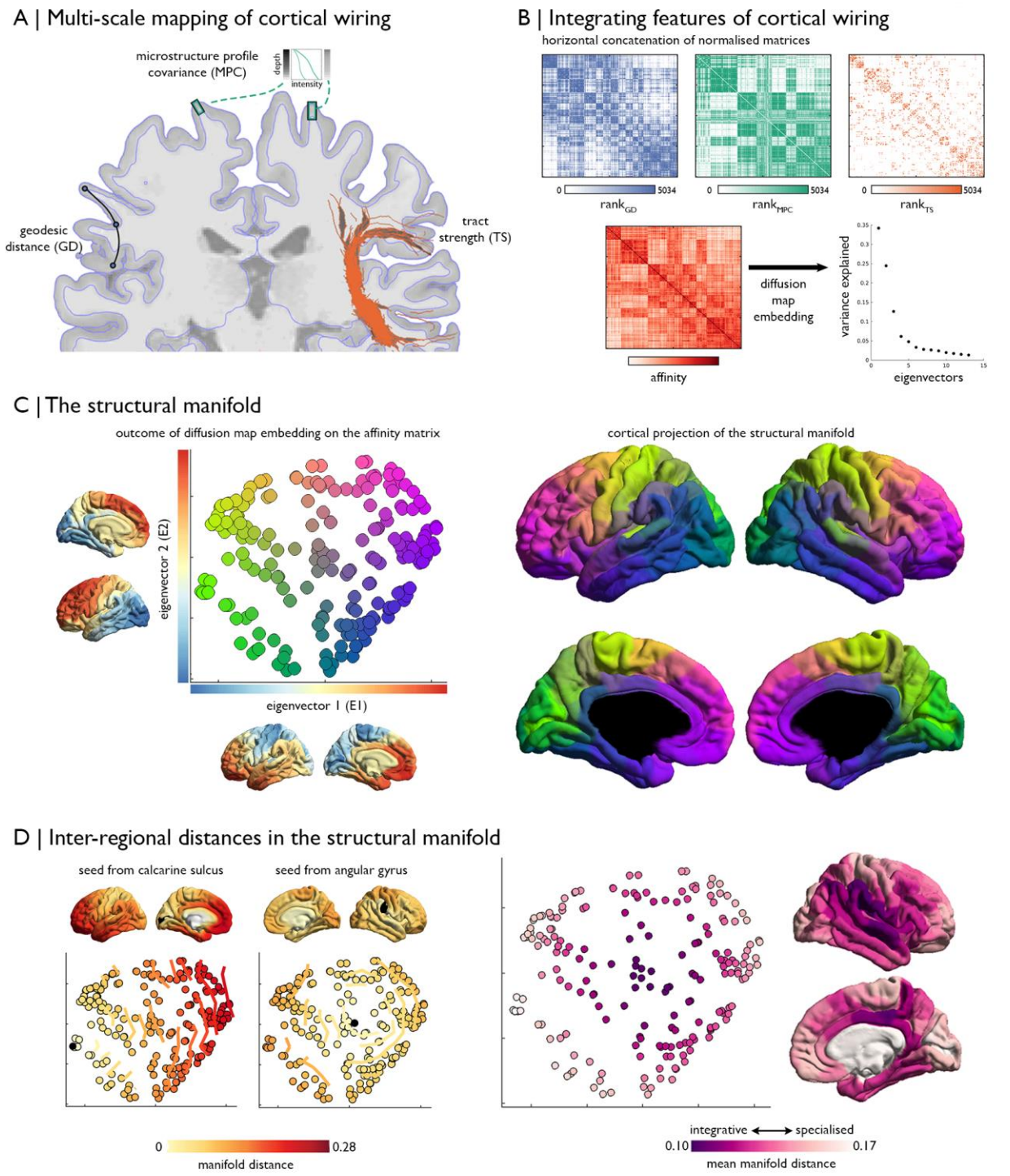

Figure 1 | The multi-scale cortical wiring model. (A) Wiring features *i.e.*, geodesic distance (GD), microstructure profile covariance (MPC), and diffusion-based tractography strength (TS) were estimated between all pairs of nodes. **(B)** Normalised matrices were concatenated and transformed into an affinity matrix. Manifold learning identified a lower dimensional representation of cortical wiring. **(C)** *Left.* Node positions in this newly-discovered structural manifold, coloured according to proximity to axis limits. Closeness to the maximum of the second eigenvector is redness, towards the minimum of the first eigenvector is greenness and towards the maximum of the first eigenvector is blueness. The first two eigenvectors are shown on the respective axes. *Right.* Equivalent cortical surface representation. **(D)** Calculation of inter-regional distances in the structural manifold from specific seeds to other regions of cortex (*left*). Overall distance to all other nodes can also be quantified to index centrality of different regions, with more integrative areas having shorter distances to nodes (*right*).

The structural manifold was generated using three complimentary features of structural connectivity, mapped between 200 spatially contiguous, evenly sized nodes: *i)* **Geodesic distance (GD),** calculated as the shortest path between two nodes stepping through white or grey matter voxels, reflects the spatial proximity and cortico-cortical wiring cost of two regions[28]; *ii)* **Microstructure profile covariance (MPC)**, that is the correlation between myelin-sensitive imaging profiles taken at each node in the direction of cortical columns[7], indexes architectonic similarity, the strongest predictor of projections in non-human primates[31]; *iii)* **Tract strength (TS)**, based on tractography applied to diffusion-weighted MRI, yields an estimate of the white matter tracts between each pair of nodes. Regional variations in the correspondence of cortical wiring features, in terms of both magnitude and direction, highlight the necessity of multi-feature integration to provide a nuanced and expressive characterisation of a region's structural connectivity (**Figure S1**).

To integrate these features into a compact model of cortical wiring, we normalised and concatenated the inter-regional matrices, computed an affinity matrix, and performed manifold learning (**Figure 1B**, see *Methods*). Diffusion map embedding, a nonlinear dimensionality reduction technique, was selected as a fast and robust approach that provides a global characterisation while preserving local structure in a fully data-driven manner[39]. Two dominant eigenvectors explained approximately 60% of variance in wiring affinity, with the first illustrating a sensory-fugal gradient (~35%) and the second an anterior-posterior gradient (~25%). These gradients represent the principle axes of variation in cortical wiring (**Figure 1C**). The two-dimensional representation is hereafter referred to as the "*structural manifold*". Distances between two nodes in this new manifold provide a single integrative metric of cortical wiring (**Figure 1D**). Nodes with high wiring affinity are close by, while dissimilar regions have a greater manifold distance. By taking the average manifold distance of each node, we found that the posterior cingulate, temporoparietal junction and superior temporal gyrus represent the integrative core of the structural manifold (**Figure 1D**). In contrast, primary sensory areas, such as the calcarine sulcus and superior precentral gyrus, exhibit highly specialised cortical wiring.

To evaluate generalizability, we reconstructed the structural manifold using an independent dataset of 40 healthy adults scanned at our imaging centre (MICA-MTL cohort; see *Methods* for details). While imaging parameters were overall comparable to the main cohort, this replication cohort involved acquisition of quantitative T1 relaxometry data to index intracortical microstructure instead of T1w/T2w maps[40–43]. Regardless of these site-wise idiosyncrasies, our procedure produced highly similar structural manifolds (correlations between both sites for eigenvectors 1/2: r=0.93/0.84, **Figure S2**). The structural manifold was also conserved at an individual level (**Figure S3**). The most prominent inter-individual shifts in nodal positioning were observed in superior temporal and superior parietal regions (**Figure S3**).

Neurobiological underpinnings

Having established a robust description of the structural manifold, we next evaluated its capacity to reflect local features of cortical wiring by examining *post mortem* human histology and gene expression data. We generated cell-staining intensity profiles for each node from a high-resolution volumetric reconstruction of a single Merker stained human brain[8] (**Figure 2A**) and extracted gene expression from mRNA sequencing data in eleven neocortical areas, each matched to one node[9,44] (**Figure 2H**). Cytoarchitectural similarity and gene co-expression were correlated to manifold distance (histology: r=-0.53, p<0.001; **Figure 2E-F**; co-expression: r=-0.64, p<0.001). Furthermore, the above associations were robust even when additionally correcting for the influence of physical distance along the cortex (histology: partial r=-0.48, p<0.001; co-expression: partial r=-0.38, p<0.001).

We hypothesised that the principle axes of the cortical wiring scheme would describe systematic variations in cytoarchitecture that reflect a region's position in a neural hierarchy. It has previously been proposed that externopyramidisation is optimally suited to assess hierarchy-dependent cytoarchitecture because it tracks the laminar origin of projections, which signifies the predominance of feedback or feedforward processing[5]. Externopyramidisation was estimated from histological markers capturing the relative density and depth of

pyramidal neurons[45] (**Figure 2C**), the primary source of interregional projections. Increasing values reflect a shift from more infragranular feedback connections to more supragranular feedforward connections[5,45]. Multiple linear regression indicated that the structural manifold was strongly correlated with externopyramidisation (r=0.69), with significance tested against 10,000 randomly rotated maps that have matched spatial autocorrelation (p_{spin}<0.001) and independent of regional variations in cortical morphology (**Figure 2G; Figure S4**). Notably, the complete model that aggregated all wiring features (*i.e.*, MPC, GD, TS) in a low dimensional structural manifold explained more variance in externopyramidisation than models constructed using alternative combinations or subsets of the wiring features (**Table S1**). Externopyramidisation gradually decreased along the second eigenvector, suggesting that our structural manifold captures a posterior to anterior transition from feedforward to feedback processing.

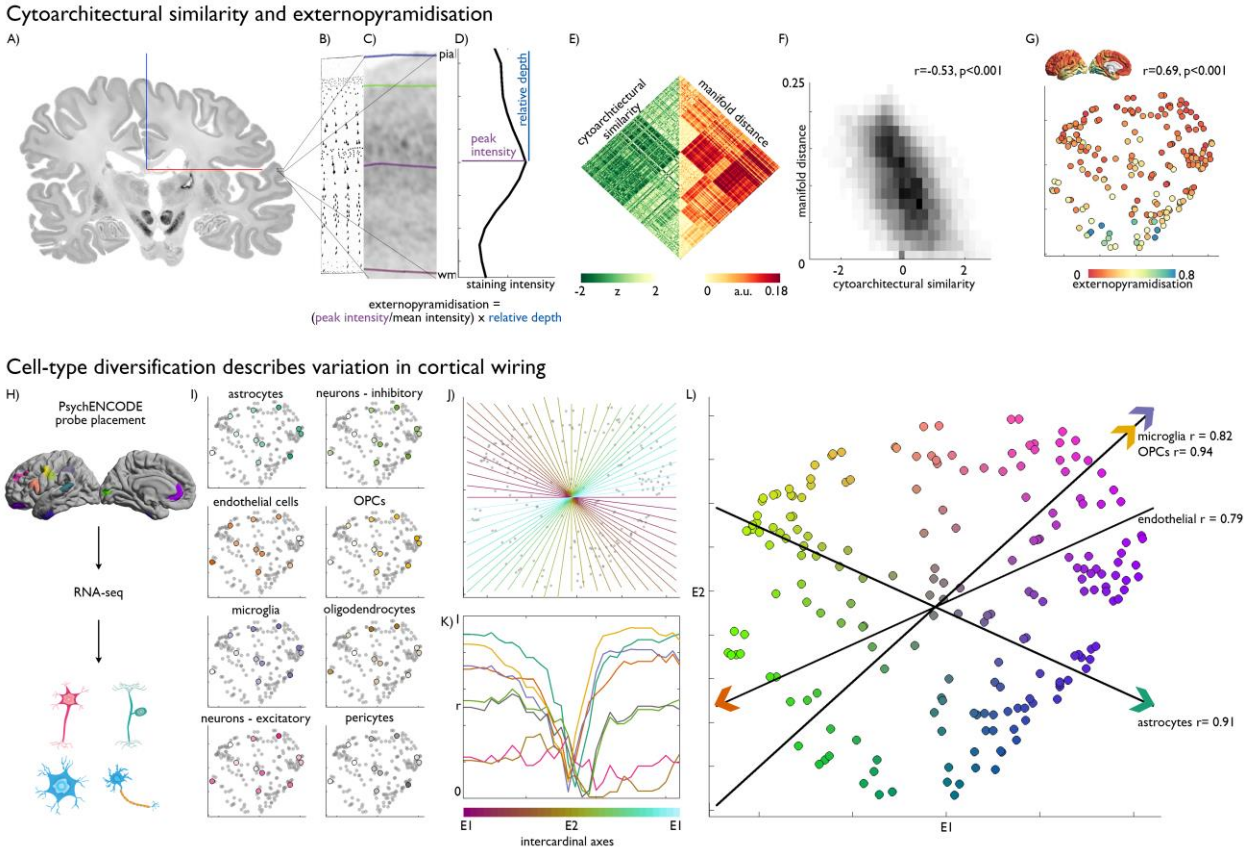

Figure 2 | Neurobiological substrates of the structural manifold. (A) Coronal slice of Big Brain, a 3D *post mortem* histological reconstruction of a human brain[8]. **(B)** Drawing of cytoarchitecture[46]. **(C)** Magnified view of cortical layers in BigBrain. **(D)** Staining intensity profile from BigBrain, with example of calculation of externopyramidisation[45]. **(E-F)** Matrix and density plot depict the correlation between BigBrain-derived cytoarchitectural similarity and manifold distance between pairs of regions. **(G)** Externopyramidisation projected onto the cortical surface and into the structural manifold. **(H)** mRNA-seq probes, assigned to eleven representative nodes (coloured as in **Figure 1C**), provided good coverage of the structural manifold and enabled characterisation of cell-type specific gene expression patterns. **(I)** Average cell-type specific gene expression patterns in the structural manifold, with brighter colours signifying higher expression. **(J)** Equally spaced intercardinal axes superimposed on the structural manifold. **(K)** Line plots showing correlation of gene expression patterns with each of the axes. **(L)** Strongest axis of variation (*i.e.*, maximum |r|) for each cell-type that passed correction for multiple comparison.

We further explored how the broader cellular composition of the cortex relates to variations in microcircuitry across the structural manifold. To do so, we estimated the expression of eight canonical cell-type gene sets in eleven cortical areas (see *Methods*) and found that these expression patterns accounted for significant variance in the macroscale organisation of cortical wiring (up to R^2=0.83, **Figure 2H-L**, **Table S2**). By defining the strongest axis of variation for each cell-type in the structural manifold, we discovered strong, distinct gradients for astrocytes

(r=0.91, p_{FDR}=0.002) and endothelial cells (r=0.79, p_{FDR}=0.033) as well as a combined oligodendrocyte precursor cells (OPCs)/microglia gradient (r=0.94/0.82, p_{FDR}=0.001/0.023) (**Figure 2I-L**). These findings established that the structural manifold captures the hierarchical organisation of non-neuronal cells (**Figure 2L**), and suggests that neuro-modulatory glia, such as astrocytes and microglia[47,48], are expressed more strongly towards the transmodal end of the structural manifold.

Functional architecture of the structural manifold

Thus far our analysis indicates that the structural manifold successfully captures features of macroscale cortical organisation, and how it relates to underlying cytoarchitectonic and cellular microcircuit properties. Next, we tested the hypothesis that the structural manifold describes how cortical wiring underpins the observed functional architecture. To this end, we mapped well established intrinsic functional communities[49] in the structural manifold and inspected manifold distances in this community structure (**Figure 3A-C**). We found that sensory networks were located in the lower (visual) and upper (somatomotor) left extremities of the structural manifold. Sensory nodes spanned a broad range of average manifold distances, reflecting transitions from specialised to integrative connectivity. In contrast, transmodal default, frontoparietal and limbic networks were located more towards the right extremities. The dorsal attention network created a frontier between sensory networks and the transmodal extremity of the structural manifold, while the ventral attention also subsumed an intermediary position at the integrative core of the structural manifold. Together, these analyses demonstrate how the relative positioning of functional communities in the structurally-derived wiring scheme underpins coordination within and between functional networks.

Next, we assessed the efficacy of our structural manifold to predict macroscale brain functional connectivity. We used a supervised machine learning paradigm that applies adaptive boosting to predict functional connectivity based on relative distances of nodes in the structural manifold (see *Methods*). The structural manifold explained substantial variance in functional connectivity across nodes (mean±SD R^2=0.58±0.15; **Figure 3D**), outperforming learners trained on data from a single modality and learners trained on all modalities but without using manifold embedding (**Figure S5**). Inspecting regional variations in R^2 scores indicated that cortical wiring topography was more tightly linked to functional connectivity in sensory areas; systems upon which classical examples of the cortical hierarchy were developed[50], while it tapered off towards high level integrative cortices. Higher inter-individual variation was associated with wither weaker structure-function coupling *i.e.*, lower variance explained in functional connectivity by the structural manifold (r=-0.34, p_{spin}<0.001). We also replicated these findings in the independent *MICA-MTL* dataset, noting slight increases in variance explained (R^2= 0.64±0.15; **Figure S2**).

To test the generalizability of structural manifold features to predict functional organisation, we assessed a *Hold-out* sample of 97 additional participants from the Human Connectome Project dataset (see *Methods*). Using the model derived from the *Discovery* dataset, we could predict functional connectivity from the structural manifold in the *Hold-out* sample within approximately one standard deviation (mean squared error=0.49±0.19, -0.19<r<1.02; **Figure 3D**). In line with the within-sample analyses, our model performed better in sensory than transmodal areas. The model also achieved high accuracy in individual subjects (mean squared error=0.89±0.25, **Figure S3**).

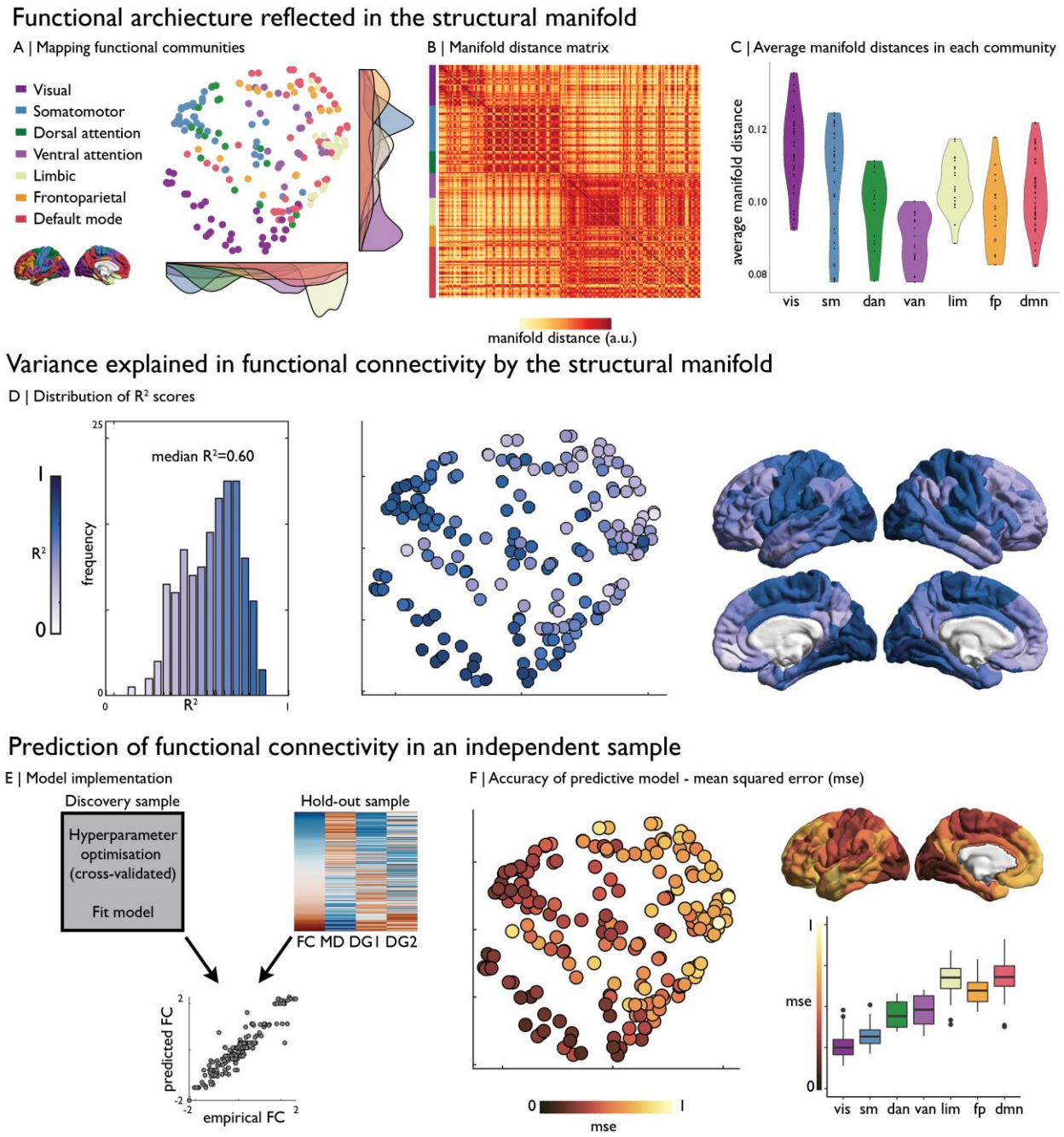

Figure 3 | From cortical wiring to functional connectivity. (A) Nodes in the structural manifold coloured by functional community[49], with the distribution of networks across the structural manifold shown by density plots along the axes. **(B)** Manifold distance between nodes, ordered by functional community, revealed a modular architecture. **(C)** Violin plots show the average manifold distance for nodes in each functional community, with lowers values in the integrative core of the structural manifold. **(D)** Variance explained in functional connectivity (FC), based on supervised learning informed by structural manifold information. The model was enacted for each node separately. R^2 values across nodes are shown in a histogram, across the structural manifold and the cortical surface. **(E)** Using the boosting regression models from D, we used features of the structural manifold to predict functional connectivity in a Hold-out sample. **(F)** Mean squared error of node-wise models shown in the structural manifold, on the cortical surface and by functional community.

Directed information processing

The above analyses showed that the structural manifold explains substantial aspects of the macroscale functional organisation and connectivity. We next examined whether it can also account for a more direct measure of neural functional connectivity, by examining stereo-electroencephalographic recordings during resting wakeful rest in ten epileptic patients (who underwent multimodal imaging before the implantations). Analysis indicated that patients presented with similar structural manifolds as controls from the same sample (**Figure S6**). We estimated coherence between all pairs of within-subject depth electrodes and examined how these were related to their location in the structural manifold (**Figure 4A**). In line with our population level functional connectivity analysis, the structural manifold model explained substantial variance in coherence (R^2=0.52±0.30; **Figure 4B; Figure S7**). We calculated the phase slope index within frequency bands (**Figure 4C)**, an estimate of unidirectional flow[51]. To account for the incomplete coverage of electrodes in each participant, we clustered the structural manifold into six macroscopic groupings (**Figure 4D**, see *Methods* for determination of k=6). We calculated the average phase slope index between each pair of clusters and performed significance testing using a linear mixed effect model that included subject as a random effect and confirmed the robustness of the results using a leave-one-subject-out procedure (**Figure 4E-F, Table S3**). The alpha band, suggested to play a role in cortico-cortical feedback processing[52], was dominated by directed coherence emanating from the somatomotor cluster (**Figure 4E**), while a premotor cluster was the second strongest driver of alpha coherence. Together, these support the importance of motor-related regions in feedback processing[53,54]. We also noted that alpha coherence shifted from the dorsal visual cluster to the ventral visual cluster, in line with a top down flow from higher order to primary visual areas. In contrast, directed gamma band coherence, indicative of feedforward processing[52], was driven from visual and paralimbic clusters, involved external and visceral sensory processing, towards frontal lobe clusters (**Figure 4F**).

Finally, we characterised the hierarchical position of clusters using a combination of the alpha and gamma phase slope index, reflecting a relative balance between feedback and feedforward processing. We estimated the propensity for feedforward processing in each cluster based on the ratio of the gamma to the absolute average across alpha and gamma phase slope indexes. This highlighted dorsal and ventral visual clusters as the origins of feedforward processing, and prefrontal, premotor, paralimbic and somatomotor clusters as preferentially feedback (**Figure 4G**). Furthermore, the hierarchical level of each cluster, defined by the mean strength of dominant direction of phase slope index, was also related to degree of externopyramidisation (**Figure 4H**). Our findings therefore establish that in the functional domain the structural manifold captures the bidirectional flow of information processing from sensory to transmodal to motor. In this way, our analysis provides novel evidence in humans for the supragranular origin of feedforward processing in unimodal regions and infragranular origin of feedback processing in transmodal regions.

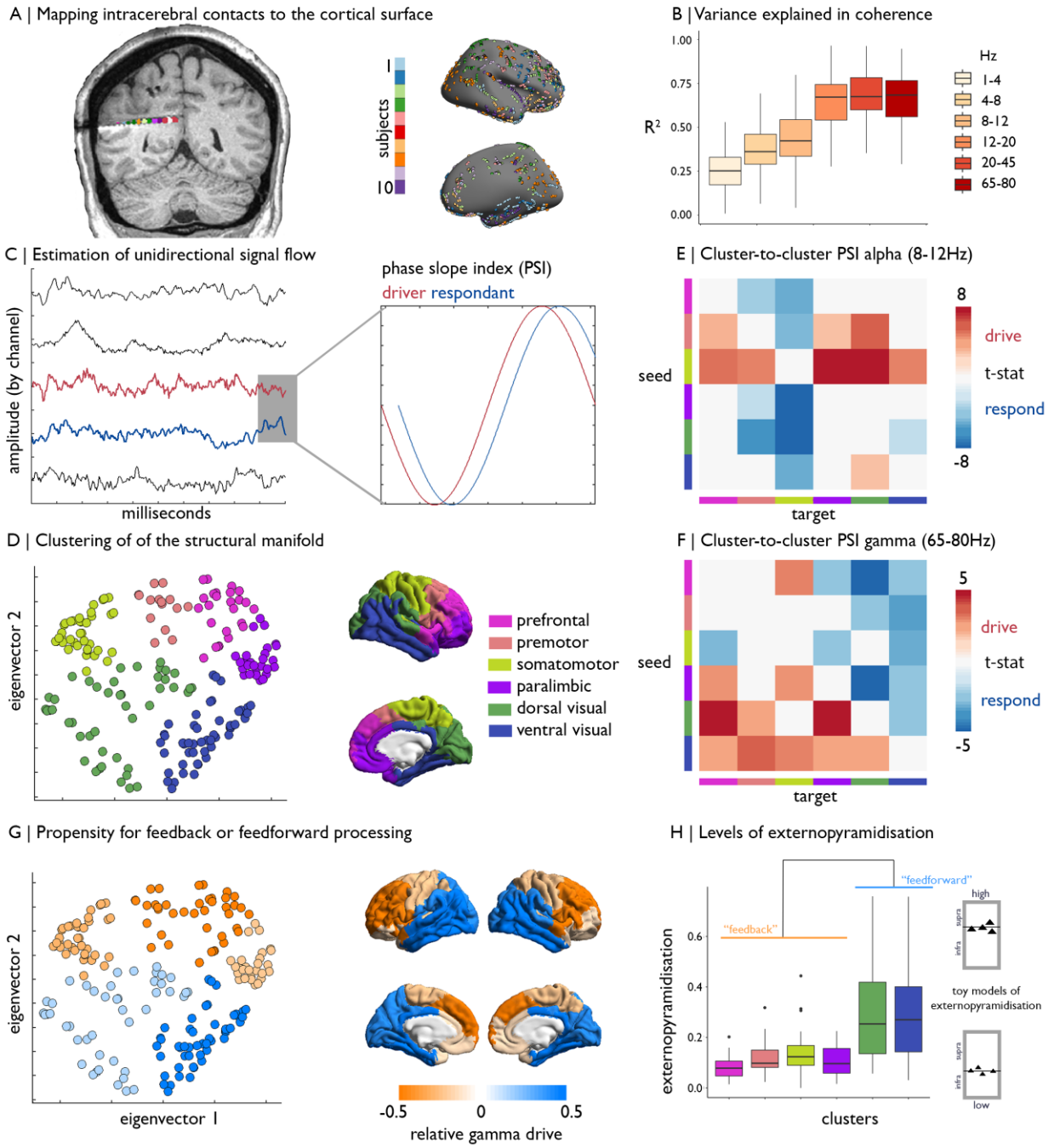

Figure 4: Hierarchical information processing is organised on the structural manifold. (A) Intracerebral implantations of ten epileptic patients were mapped to cortical surface. Intracortical EEG recordings were selected across five minutes of rest. **(B)** Boxplots show the variance explained in coherence by the structural manifold using adaboost machine learning across all nodes. **(C)** The phase slope index (PSI), an estimate of directional coherence, was calculated for each pair of intra-participant electrodes[51], then mapped to clusters of the structural manifold **(D)**. **(E-F)** PSI estimates between these clusters in alpha and gamma frequency bands are represented as a seed x target matrices, thresdholed as q<0.05 FDR corrected. **(G)** Cluster-wise propensity for gamma driving PSI, taken as the ratio of mean gamma PSI and mean absolute PSI across alpha and gamma. **(H)** Boxplots show the shift in the level of externopyramidisation in alpha dominant "feedback" vs gamma dominant "feedforward" dominant clusters, with toy models of the cytoarchitectural picture of high and low externopyramidisation.

DISCUSSION

Based on advanced machine learning of multiple features of cortical structure, our work identified a compact and data-driven representation of the wiring of human cortex. Our analysis established that cortical wiring is dominated by two principal axes, one running from sensory towards transmodal systems and one running from anterior to posterior. Critically, this novel structural manifold space successfully accounted for both local descriptions of cortical microcircuitry as well as macroscale cortical functional dynamics measured by functional MRI and intracranial electrical recordings. By projecting *post mortem* histological and transcriptomic profiles into this newly discovered space, we could demonstrate how these axes are determined by a blueprint of intersecting cell-type specific and microcircuitry gradients. In addition to establishing these local neurobiological features, our findings support that the structural manifold serves as a powerful scaffold within which macroscale cortical function can be understood. Using both non-invasive imaging in healthy individuals, and direct neuronal measurements in a clinical population, we demonstrated that the structural manifold describes how neural function is hierarchically organised in both space and time. Our findings were replicable in different datasets and at the single subject level; moreover, a series of additional experiments shows that this novel representation is superior to conventional approximations of structural connectivity. Together, we have successfully identified a compact description of the wiring of the cortex that can help to ultimately understand how neural function is simultaneously constrained by both local and global features of cortical organisation.

Our multivariate model of cortical wiring reflects an important extension on diffusion MRI tractography because it additionally incorporates spatial proximity and microstructural similarity, both features tap into generative principles of cortico-cortical connectivity as demonstrated by prior human and non-human animal studies[32–35]. The application of manifold learning to this enriched representation of cortical wiring helped to determine a low dimensional, yet highly expressive, depiction of cortical wiring. In other fields, notably genomics and data science more generally, embedding techniques have become widely adopted to identify and represent the structure in complex, high-dimensional datasets[9,39,55,56]. In recent neuroimaging studies, several approaches have harnessed non-linear dimensionality reduction techniques to identify manifolds from single modalities, highlighting changes in microstructure and function at the neural system level[7,37,57,58]. The structural manifold identified here captured both sensory-fugal and anterior-posterior processing streams, two core modes of cortical organisation and hierarchies established by seminal tract-tracing work in non-human primates[36,59]. The anterior-posterior axis combines multiple local gradients and functional topographies, such as the ventral visual stream running from the occipital pole to the anterior temporal pole that implements a sensory–semantic dimension of perceptual processing[60,61] and a rostro-caudal gradient in the prefrontal cortex that describes a transition from high-level cognitive processes supporting action preparation to those tightly coupled with motor execution[59,62–64]. The sensory-fugal axis represents an overarching organisational principle that unites these local processing streams. While consistent across species, the number of synaptic steps from sensory to higher order systems has increased throughout evolution, supporting greater behavioural flexibility[36] and decoupling of cognitive functioning from the here and now[61]. By systematically studying inter-nodal distances within the structural manifold, it may be possible to gain a more complete understanding of the difference between specialised systems at the periphery and more centrally localised zones of multimodal integration, such as the temporo-parietal junction and cingulate cortex. Many of these regions have undergone recent evolutionary expansion[65], are sites of increased macaque-human genetic mutation rates[66], and exhibit the lowest macaque-human functional homology[67]. In this context, the more complete model of cortical wiring provided by our structural manifold may play a critical role in advancing our understanding of how changes in cortical organisation have given rise to some of the most sophisticated features of human cognition.

Our manifold reflects an intermediate description of cortical organisation that simultaneously describes the microstructural underpinnings that give rise to macroscale organisation and to also address the emergence of functional dynamics and hierarchies at the system level. Cross-referencing the structural manifold with a 3D histological reconstruction of a human brain[8], established the close correspondence between our *in vivo* model and histological measurements of the cortical microcircuitry. This work adds to the notion that cytoarchitecture and cortical wiring are inherently linked[68,69], as variations in projections across cortical layers determine the layout of the cortical microcircuitry[70]. Feedforward connections often originate in supragranular layers (and terminate in lower layers in the target regions), while infragranular layers give rise to feedback projections flowing down the cortical hierarchy[71–74]. In this work, we observed an alignment between the cortical wiring scheme and a proxy for externopyramidisation[45], which was sensitive to inter-areal differences in the depth of peak pyramidal neuron density that co-occurs with shifts from feedback to feedforward dominated connectivity profiles[5]. In addition to

showing cytoarchitectonic underpinnings of the cortical microcircuitry, we capitalised on *post mortem* gene expression datasets derived from mRNA sequencing[75], a technique thought to be more sensitive and specific than microarray transcriptomic techniques. This approach revealed that divergent gradients of cell type-specific gene expression underpin intercardinal axes of the structural manifold, particularly of non-neuronal cell types. Increased glia-to-neuron ratios in transmodal compartments of the structural manifold may support higher order cognitive functions, given comparative evidence showing steep increases in this ratio from worms to rodents to humans[76–79]. Astrocytes, in particular, exhibit morphological variability that may lend a cellular scaffold to functional complexity and transmodal processing[76]. For example, a uniquely human inter-laminar astrocyte was recently discovered with long fibre extensions, likely supporting long-range communication between distributed areas that may contribute to flexible, higher-order cognitive processing[80].

Our manifold description of cortical wiring also provides a coordinate system that establishes how structural constraints give rise to cortical dynamics and information flow throughout hierarchical and modular systems. We could show that functional communities are circumscribed within the structural manifold, supporting dense within-network connectivity, and that their relative positions describe a progressive transition from specialised sensory wiring to an integrative attentional core and distributed transmodal networks. Region-to-region distances in the structural manifold provided robust predictions of resting-state functional connectivity data, both at the level of the group and of a single subject. Spatial proximity and microstructural similarity are critical elements of the predictive value of our models, highlighting the importance of intracortical and cytoarchitecturally-matched projections in shaping intrinsic functional organization. However, these dominant aspects of cortical wiring are often not considered by computational models that simulate functional connectivity from measures of diffusion-based tractography[19,20,81]. In addition to feature enrichment, the use of nonlinear dimensionality reduction enhanced the predictive performance by minimising the influence of noisy edges and magnifying effects from the most dominant axes of cortical wiring. Such a model led to maximal gains in predictive power in unimodal areas, likely owing to their more locally clustered, and hierarchically governed connectivity profiles[82–84]. Predictive performance decreased towards transmodal networks, a finding indicating that more higher-level systems may escape (currently measurable) structural constraints. Such conclusions are in line with recent work showing that transmodal areas exhibit lower microstructure-function correspondence[7] and reduced correlations between diffusion tractography and resting state connectivity[85,86], potentially contributing to greater behavioural flexibility[7,87]. The hierarchical nature of the structural manifold was further supported by analysing its correspondence to direct measurements of neural dynamics and information flow via intracerebral stereo-electroencephalography. Specifically, we could demonstrate that manifold topology mirrors the stream of neural information propagation from externally- and viscerally-focused areas, which selectively drive gamma oscillations towards frontal areas as well as the dominance of the motor-related areas in driving feedback throughout the cortex. The clear patterns of directed coherence in these frequency bands aligns with evidence of the selective involvement of alpha and gamma oscillations in feedback and feedforward processing[73,88,89]. Directed coherence between regions was often bidirectional across these frequency bands, thereby showing how neuronal communication occurs separately in both directions of the hierarchy[90]. One key feature of the present framework, therefore, is that it provides a basis to quantitatively assess how the interplay of neuronal oscillations underpin complex human behaviors. Even with limited spatial resolution, data-driven decomposition of the structural manifold proved an effective model of electrophysiological organization, in line with recent work showing the modular architecture of electrocorticography[91]. Although these findings were obtained in only a small group of neurological patients, they were again consistent at the single subject level.

As our results have shown, our manifold representation of cortical connectivity provides a practical workspace to interrogate the coupling of brain structure and function, and the links between microcircuit properties and macroscale hierarchies. As such, the structural manifold may offer novel perspectives to study brain development and aging, and to assess perturbations in prevalent disorders. In an effort to provide our community access to the methods we used here, we have made normative manifold maps openly available (https://github.com/MICA-MNI/micaopen/tree/master/structural_manifold) and incorporated all relevant functions and workflow into the BrainSpace toolbox (http://brainspace.readthedocs.io[92]).

METHODS

Human Connectome project dataset

a) Data Acquisition

We studied data from 197 unrelated healthy adults from the S900 release of the Human Connectome Project (HCP; Glasser et al., 2013). The *Discovery* dataset included 100 individuals (66 females, mean±SD age=28.8±3.8 years) and the *Hold-out* dataset included 97 individuals (62 females, mean±SD age=28.5±3.7 years). MRI data were acquired on the HCP's custom 3T Siemens Skyra equipped with a 32-channel head coil. Two T1w images with identical parameters were acquired using a 3D-MPRAGE sequence (0.7mm isotropic voxels, matrix=320×320, 256 sagittal slices; TR=2400ms, TE=2.14ms, TI=1000ms, flip angle=8°; iPAT=2). Two T2w images were acquired using a 3D T2-SPACE sequence with identical geometry (TR=3200ms, TE=565ms, variable flip angle, iPAT=2). A spin-echo EPI sequence was used to obtain diffusion weighted images, consisting of three shells with *b*-values 1000, 2000, and 3000s/mm^2 and up to 90 diffusion weighting directions per shell. (TR=5520ms, TE=89.5ms, flip angle=78°, refocusing flip angle=160°, FOV=210×180, matrix=178×144, slice thickness=1.25mm, mb factor=3, echo spacing=0.78ms). Four rs-fMRI scans were acquired using multi-band accelerated 2D-BOLD echo-planar imaging (2mm isotropic voxels, matrix=104×90, 72 sagittal slices, TR=720ms, TE=33ms, flip angle=52°, mb factor=8, 1200 volumes/scan). Participants were instructed to keep their eyes open, look at fixation cross, and not fall asleep. While T1w, T2w and diffusion scans were acquired on the same day, rs-fMRI scans were split over two days (two scans/day).

b) Data preprocessing

MRI data underwent HCP's minimal preprocessing [93]. Cortical surface models were constructed using Freesurfer 5.3-HCP [94–96], with minor modifications to incorporate both T1w and T2w [97]. Following intensity nonuniformity correction, T1w images were divided by aligned T2w images to produce a single volumetric T1w/T2w image per subject, a contrast ratio sensitive to cortical microstructure (Glasser and Van Essen, 2011). Diffusion MRI data underwent correction for geometric distortions and head motion [93]. BOLD timeseries were corrected for gradient nonlinearity, head motion, bias field and scanner drifts, then subjected to ICA-FIX for removal of additional noise [98]. The rs-fMRI data were transformed to native space and timeseries were sampled at each vertex of the MSMAll registered midthickness cortical surface [99,100].

c) Generation of the wiring features

Cortical wiring features were mapped between 200 spatially contiguous cortical 'nodes'. The parcellation scheme preserves the boundaries of the Desikan Killany atlas [101] and was transformed from fsaverage7 to subject-specific cortical surfaces via nearest neighbour interpolation.

Geodesic distance

Geodesic distance (GD) was calculated across subject-specific mid-cortical surface maps in native space. Exemplar vertices of each node were defined for each subject as the vertex with minimum Euclidian distance to the subject-specific node centroid. For each node, we matched the exemplar vertex to the nearest voxel in volumetric space, then used a Chamfer propagation (imGeodesics Toolbox; https://github.com/mattools/matImage/wiki/imGeodesics) to calculate the distance to all other voxels travelling through a grey/white matter mask. This approach differs from previous implementations of geodesic distance[28,29,37] by involving paths through the grey and white matter, allowing for jumps within gyri and interhemispheric projections[102]. We projected GD estimations back from volumetric to surface space, averaged within node and produced a 200×200 GD matrix.

Microstructure profile covariance

The full procedure of the MPC approach may be found elsewhere[7]. In brief, we generated 12 equivolumetric surfaces between the outer and inner cortical surfaces[103], and systematically sampled T1w/T2w values along linked vertices across the whole cortex. T1w/T2w intensity profiles were averaged within nodes, excluding outlier vertices with median intensities more than three scaled median absolute deviations away from the node median intensity. Nodal intensity profiles underwent pairwise Pearson product-moment correlations, controlling for the average whole-cortex intensity profile. The MPC matrix was absolutely thresholded at zero; remaining MPC values were then log-transformed to produce a symmetric 200×200 MPC matrix.

Tract strength

Tractographic analysis was based on MRtrix3 (https://www.mrtrix.org). Response functions for each tissue type were estimated using the dhollander algorithm[104]. Fibre orientation distributions were modelled from the diffusion-weighted MRI with multi-shell multi-tissue spherical deconvolution[105] and subsequently underwent multi-tissue informed log-domain intensity normalisation. Anatomically constrained tractography was performed systematically by generating streamlines using second order integration over fibre orientation distributions with dynamic seeding[106,107]. Streamline generation was aborted when 40 million streamlines had been accepted. Using a spherical-deconvolution informed filtering of tractograms (SIFT2) approach, interregional tract strength (TS) was taken as the streamline count weighted by the estimated cross section[107]. A group-representative 200×200 TS matrix was generated using distance dependent consensus thresholding[108]. The approach involves varying the consensus threshold as a function of distance. The resulting connectivity matrix preserves the pooled edge length distribution of subject-level data as well as integral organisational features, such as long-range connections, while reducing false positive edges. The group-representative matrix contained 13.7% of possible edges.

Correspondence of cortical wiring features

To assess the complementariness of these features in characterising cortical wiring, we computed matrix-wide Spearman correlations between all feature pairs (MPC-GD, MPC-TS, GD-TS). We also assessed regional variations in feature correspondence at each node using Spearman correlations and the standard deviation in a multi-feature fingerprint (**Figure S1**).

d) Building the structural manifold

Overview of approach

The structural manifold was built through the integration of MPC, GD, and TS. The procedure can be implemented via the openly available BrainSpace toolbox[92], and is as follows:

i) **Normalisation:** Nonzero entries of the input matrices were rank normalised. Notably, rank normalisation was performed on the inverted form of the GD matrix *i.e.,* larger values between closer regions. The less sparse matrices (GD and MPC) were rescaled to the same numerical range as the sparsest matrix (TS) to balance the contribution of each input measure.

ii) **Fusion:** Horizontal concatenation of matrices and production of a node-to-node affinity matrix using row-wise normalised angle similarity. The affinity matrix thus quantifies the strength of cortical wiring between two regions. Alternative data fusion techniques, such similarity network fusion[109] and joint embedding[67], aim to identify similar motifs across modalities. A key outcome of those approaches is higher signal-to-noise ratio, however, unique network information provided by each modality would be minimised. Given our cross-modal structural analyses highlighted special principles of cortical organisation are represented by each modality, we sought to use the concatenation approach that preserves distinct information in each modality.

iii) **Manifold learning:** Diffusion map embedding was employed to gain a low dimensional representation of cortical wiring. Diffusion map embedding belongs to the family of graph Laplacians, which involve

constructing a reversible Markov chain on an affinity matrix. Compared to other nonlinear manifold learning techniques, the algorithm is robust to noise and computationally inexpensive[110,111]. A single parameter α controls the influence of the sampling density on the manifold (α = 0, maximal influence; α = 1, no influence). As in previous studies[37,112], we set α = 0.5, a choice retaining the global relations between data points in the embedded space. Notably, different alpha parameters had little to no impact on the first two eigenvectors (spatial correlation of eigenvectors, r>0.99). We operationalised a random walker to approximate the likelihood of transitions between nodes, illuminating the local geometry in the matrix. Preservation of local geometry using the kernel critically differentiates diffusion maps from global methods, such as principle component analysis and multidimensional scaling. Local geometries are integrated into a set of global eigenvectors by running the Markov chain forward in time. The decay of an eigenvector provides an integrative measure of the connectivity between nodes along a certain axis. This lower dimensional representation of cortical wiring is especially interesting for interrogating the cortical hierarchy, which previous research suggests extends upon sensory-fugal and anterior-posterior axes. In the present study, the number of dimensions selected for further analysis was determined based on the variance explained by each eigenvector, where the cut-off point determined using the Cattell scree test. This resulted in two dimensions, which aligns with the hypothesised number of axes and, fortunately, can be readily interpreted.

Key outcome metrics

The structural manifold represents the principle axes of variation in cortical wiring, as well as their interaction. We displayed the conversion from anatomical to structural manifold using a three-part colourmap. The colour of each node was ascribed based on proximity to the limits of the structural manifold; blue for closeness to the maximum of the first eigenvector, green for closeness to minimum of the first eigenvector, and redness represents closeness to maximum of the second eigenvector.

The relative positioning of nodes in the structural manifold informs on the strength of cortical wiring along the principle axes. We characterised the relative positioning of each pair of nodes with manifold distance and difference along each primary axis, which pertain to node-to-node proximity and axis-specific shifts, respectively. To calculate manifold distances, we triangulated the structural manifold used a Delaunay approach and calculated geodesic distance between each node used the Fast Marching Toolbox (https://github.com/gpeyre/matlab-toolboxes/tree/master/). The average manifold distance of each node informs upon centrality within the space and reflects a region's propensity to have many cortical connections.

Neurobiological substrates of structural manifold

a) Association to cytoarchitectural features. For the cytoarchitectonic maps, a 100μm resolution volumetric histological reconstruction of a *post mortem* human brain from a 65-year-old male was obtained from the open-access BigBrain repository[8], on February 2, 2018 (https://bigbrain.loris.ca/main.php). Using previously defined surfaces of the layer 1/11 boundary, layer 4 and white matter[113], we divided the cortical mantle into supragranular (layer 1/11 to layer 4) and infragranular bands (layer 4 to white matter). Staining intensity was sampled along five equivolumetric surfaces within the predefined supra- and infra-granular bands at 163,842 matched vertices per hemisphere, then averaged for each parcel. We estimated cytoarchitectural similarity of regions by performing the above MPC procedure on BigBrain derived intracortical profiles, as in previous work[7]. Externopyramidisation[45], described as the "gradual shift of the weight of the pyramidal layers from the V to the IIIc", was approximated as the product of the normalised peak intensity and the relative thickness of the supragranular layers, i.e.

$$\text{Externopyramidisation} = \frac{\max(intensity)}{\text{mean}(intensity)} \times \frac{1 - thickness_{supra}}{thickness_{total}}$$

Intensity and thickness quotients were independently rescaled between 0 and 1 across all regions to balance their contribution to the externopyramidisation metric. Higher values reflect higher intensity values and shallower depth of the peak layer.

b) Cell-type specific gene expression. Cell-type specific gene lists were derived from an analysis of >60,000 single cells extracted from human adult visual cortex, frontal cortex, and cerebellum with single-nucleus Droplet-based sequencing (snDrop-seq) or single-cell transposome hypersensitive-site sequencing (scTHS-seq)[114]. We focused on eight canonical cell classes; astrocytes, endothelial cells, microglia, inhibitory neurons, excitatory neurons, oligodendrocytes, OPCs, and pericytes. Cell-type specific expression maps were calculated as the average of log2 normalised gene expression across eleven neocortical areas in twelve human adult brains[9,44]. Areas were visually matched to the nearest parcel. Inter-regional co-expression was calculated as the Spearman correlation between cell-type specific gene expression.

The influence of neurobiological similarities on relative positioning of nodes in the structural manifold was tested by performing Spearman correlations of manifold distance with cytoarchitectural similarity and cell type specific gene co-expression patterns, with and without controlling for geodesic distance. We used multiple linear regressions to evaluate the variance explained in externopyramidisation and cell-type specific expression by the two structural manifold eigenvectors. Significance values were corrected to account for spatial autocorrelation in the eigenvectors using spin testing and Moran spectral randomisation, respectively[116,117], and was operationalised using BrainSpace[92]. Spectral randomisation was initialised using the geodesic distance matrix. As an additional control analysis, we tested the correspondence of the first two eigenvectors with features of cortical morphometry using the same procedure.

The structural manifold offers a dimensional approach to evaluate the concordance of gradients at multiple biological scales. To facilitate multi-scale comparisons, we generated 32 axes within the structural manifold by creating inter-cardinal lines in 5.625° steps. Linear polynomial equations, corresponding to each inter-cardinal line, were evaluated for 100 equally spaced x and y-values between the minimum and maximum range of the first and second eigenvectors, respectively. Nodes were assigned the values of the nearest point along each inter-cardinal line, based on Euclidean distance, thus the position of a node on each axis could be represented by an integer (1 – 100). The dominant axis of variation of any feature in structural manifold can be classified as the axis of maximum correlation. P-values from the Spearman correlations were subjected to FDR correction to assess whether the dominant axis of variation was significant[118].

Association to resting-state functional connectivity

Functional architecture

The structural manifold was reimagined as a completely dense network with edges weighted by manifold distance (**Figure 3F**). We mapped seven established functional communities[49] into the group-level structural manifold by assigning each node to the functional community that was most often represented by the underlying vertices.

Predicting functional connectivity

Individual functional connectomes were generated by averaging preprocessed timeseries within nodes, correlating nodal timeseries and converting them to z scores. For each individual, the four available rs-fMRI scans were averaged at the matrix level, then the connectomes were averaged within the Discovery and Hold-out samples separately. We estimated the variance explained in functional connectivity by the cortical wiring scheme using boosted regression trees. Boosted regression trees produce a predictive model from the linear weighted combination of weaker base learners that each fit the mean response of a subsection of the predictor space. Weak estimators are built in a step-wise manner, with increasing focus on poorly explained sections of the predictor space. Optimisation of the learning rate and number of estimators is critical to model complex nonlinear relationships, implicitly model interactions between predictors, and reduce overfitting. Overfitting was further reduced and predictive performance enhanced by using a random subset of data to fit each new tree. The present study specifically used the AdaBoost

module of scikit-learn v0.21.3in Python3.5 and established the optimal number of estimators and the learning rate using internal five-fold cross-validation [maximum tree depth = 4, number of estimators = 6:2:20, learning rate = (0.01, 0.05, 0.1, 0.3, 1); see **Figure S5** for node-wise hyperparameters]. We aimed to predict functional connectivity independently for each node based on manifold distance, difference along the first eigenvector and difference along the second eigenvector to all other nodes. We assessed the variance explained (R^2) in group-level functional connectivity within the *Discovery* dataset, then using the same model parameters calculated mean squared error between empirical and predicted functional connectivity in the *Hold-out* dataset.

Replication of the structural manifold in an independent dataset

Independent replication was performed using locally acquired data from 40 healthy adults (MICA-MTL cohort; 14 females, mean±SD age=30.4±6.7, 2 left handed) for whom quantitative T1 relaxation time mapping (qT1) images were available. All participants gave informed consent and the study was approved by the local research ethics board of the Montreal Neurological Institute and Hospital. MRI data was acquired on a 3T Siemens Magnetom Prisma-Fit with a 64-channel head coil. A submillimetric T1-weighted image was acquired using a 3D-MPRAGE sequence (0.8mm isotropic voxels, 320x320 matrix, 24 sagittal slices, TR=2300ms, TE=3.14ms, TI=900ms, flip angle=9°, iPAT=2) and qT1 data was acquired using a 3D-MP2RAGE sequence (0.8mm isotropic voxels, 240 sagittal slices, TR=5000ms, TE=2.9ms, TI 1=940ms, T1 2=2830ms, flip angle 1=4°, flip angle 2=5°, iPAT=3, bandwidth = 270 Hz/px, echo spacing = 7.2ms, partial Fourier = 6/8). The combination of two inversion images in qT1 mapping minimises sensitivity to B1 inhomogeneities [42], and provides high intra-subject and inter-subject reliability [119]. A spin-echo EPI sequence was used to obtain diffusion weighted images, consisting of three shells with b-values 300, 700, and 2000s/mm2 and 10, 40, and 90 diffusion weighting directions per shell, respectively (TR=3500ms, TE=64.40ms, 1.6mm isotropic voxels, flip angle=90°, refocusing flip angle=180°, FOV=224×224 mm^2, slice thickness=1.6mm, mb factor=3, echo spacing=0.76ms). One 7 min rs-fMRI scan was acquired using multi-band accelerated 2D-BOLD echo-planar imaging (TR=600ms, TE=30ms, 3mm isotropic voxels, flip angle=52°, FOV=240×240mm^2, slice thickness=3mm, mb factor=6, echo spacing=0.54mms). Participants were instructed to keep their eyes open, look at fixation cross, and not fall asleep.

The data preprocessing and construction of the structural manifold were otherwise virtually identical to the original Human Connectome Project dataset, with a few exceptions. Microstructure profiles were sampled from qT1 images. Cortical surface estimation via FreeSurfer utilised two T1 scans, and surface models were manually edited for accuracy. The rs-fMRI data was denoised using an in-house trained ICA-FIX classifier[98,120] as well as spike regression. Timeseries were sampled on native cortical surfaces and resampled to fsaverage via surface-based registration.

Intracranial EEG analyses in epileptic patients

A group of ten patients with drug-resistant focal epilepsy (one male, mean±SD age=28.9±7.9, all right handed) were scanned using the same imaging protocol as the heathy controls from the *Replication* dataset. Patients furthermore underwent intracerebral stereo-electroencephalographic investigation as part of their presurgical evaluation, after the imaging. The protocol received prior approval from the MNI Institutional Review Board. The recordings were acquired with Nihon Khoden EEG amplifiers at a sampling rate of 2000Hz, using 1 single type of depth electrodes (DIXI electrodes with either 10 or 15 electrode). A board certified neurophysiologist (BF) selected epochs without ictal events, absent of artefacts, from periods of resting wakefulness with eyes closed during standardised conditions; resulting in 1-2 minutes of recording for each patient.

Each depth electrode was mapped to a cortical parcel using with the following procedure. For each subject, cortical surfaces were extracted from the high-resolution pre-implantation T1-weighted using FreeSurfer6.0. Next, a clinical structural image, acquired during the implantation period on a Philips Medical Systems 1.5T MRI scanner, was transformed to the T1-weighted space using volume-based affine transformation with nearest neighbour

interpolation. For seven patients, the clinical scan was a T1-weighted image (T1_3D_SENSE, slice thickness=0.78mm, number of slices =280, single echo, phase encoding steps = 320, echo train length = 320, TR=0.0079s, flip angle = 6°, multi coil receiver coil, TE=0.0035s). For three subjects, the clinical scan was an Axial T2 scan (slice thickness=2mm, number of slices=242, single echo, echo train length=141, TR=2.8, flip angle = 90°, multi coil receiver coil, TE=0.48s). Each electrode in grey matter was mapped to the nearest surface vertex, and labelled as the corresponding parcel, based on minimum geodesic distance from the centroid coordinate of the electrode to the cortical midsurface.

Directed information processing

Intracranial EEG signals were re-referenced to the average signal of grey matter channels. The auto spectral density of each channel, P_{xx}, and the cross power spectral density between pairs of within-subject channels, P_{xy}, were calculated with Welch's method (59 overlapping blocks, 2s duration, 1s steps, weighted by Hamming window). These measures allow for the magnitude squared calculation of coherence between two signals [121,122]

$$C_{xy}(f) = P(f)_{xy}^2 \,/\, P(f)_{xx}P(f)_{yy}$$

In the above formula, P_{xx} and P_{yy} are power spectral density estimates and P_{xy} is the cross spectral density estimate. Coherence was evaluated in 0.77 Hz steps (n=129) from 0.5-100Hz, then averaged within six frequency bands [1-4, 4-8, 8-12, 12-20, 20-45, 65-80 Hz]. The band 45-65 Hz was not analysed due to line noise at 60 Hz. Within each individual, we performed Adaboost regression to estimate variance explained in coherence by the subject-specific structural manifold as before [see *Predicting Functional Connectivity* for details]. In contrast to the fMRI-analysis, however, all nodes and connections were estimated within one global model per subject.

The temporal coupling of two signals was determined by the phase-slope index, using the formula:

$$\psi_{xy} = \Im\left(\sum_{f \in F} C_{xy}^{*}(f) C_{xy}(f + \delta f)\right)$$

In the above formula, C_{xy} is complex coherence as defined above, δf is the frequency resolution, $\Im(\cdot)$ denotes taking the imaginary part and F is the set of frequencies over which the slope is summed [51]. Given incomplete coverage of intracranial electrodes in each subject, we discretised the structural manifold into a set of sub-sections using consensus k-means clustering. Consensus-based k-means clustering and converged on a stable solution of k=6 across 100 repetitions[123]. We used a linear mixed effect models to approximate the relationship between phase-slope index within each frequency band and cluster membership:

$$\Psi \sim categorical(EdgeType) + md + \Delta e1 + \Delta e2 + (1|subject) + (1|channel_{seed}) + (1|channel_{target}) + \varepsilon$$

Here, Ψ stands for phase slope index and *EdgeType* was defined by the seed and target clusters, in such that the *EdgeType* of a connection from cluster 1 to cluster 2 would be '12'. *EdgeType* was a fixed effect, *subject* and *channels* were nested in the model with random intercepts. We also included manifold distance (*md*), difference on eigenvector 1 (*Δe1*) and difference on eigenvector 2 (*Δe2*) as fixed effects to account for variations in the positioning on nodes within a cluster. We used the t-statistics of each *EdgeType* category as a measure of phase slope index between clusters. The significance of each *EdgeType* effect was determined using FDR correction on the fixed effect p-values of linear mixed effect model with an alpha level of 0.05. Standard deviations in the t-statistics were quantified across leave-one-subject-out iterations to ensure robustness of the direction and strength of the phase slope index estimates. Preprocessing was performed using the FieldTrip toolbox [124], while the cross-spectral density estimates, phase slope index and linear models were estimated using MATLAB [125].

Code and data availability statements

Preprocessed group-level matrices, normative manifold maps and integral scripts are openly available at https://github.com/MICA-MNI/micaopen/tree/master/structural_manifold

Acknowledgements

The authors would also like to express their gratitude to the open science initiatives that made this work possible, including the teams involved in the BigBrain project, the PsychEncode consortium, the Human Connectome Project and Scikit-learn. Furthermore, we thank Dr. Matthias Kirschner for his helpful insight on the manuscript, and the MRI and EEG technicians at the Montreal Neurological Institute.

REFERENCES

1. Mountcastle, V. B. The columnar organization of the neocortex. *Brain* **120**, 701–722 (1997).
2. Sporns, O. The human connectome: A complex network. *Annals of the New York Academy of Sciences* **1224**, 109–125 (2011).
3. Charvet, C. J. & Finlay, B. L. Evo-devo and the primate isocortex: the central organizing role of intrinsic gradients of neurogenesis. *Brain. Behav. Evol.* **84**, 81–92 (2014).
4. Fulcher, B. D., Murray, J. D., Zerbi, V. & Wang, X.-J. Multimodal gradients across mouse cortex. *Proc. Natl. Acad. Sci.* **116**, 4689–4695 (2019).
5. Goulas, A., Zilles, K. & Hilgetag, C. C. Cortical Gradients and Laminar Projections in Mammals. *Trends in Neurosciences* **41**, 775–788 (2018).
6. García-Cabezas, M., Joyce, M. K. P., John, Y. J., Zikopoulos, B. & Barbas, H. Mirror trends of plasticity and stability indicators in primate prefrontal cortex. *Eur. J. Neurosci.* **46**, 2392–2405 (2017).
7. Paquola, C. *et al.* Microstructural and functional gradients are increasingly dissociated in transmodal cortices. *PLOS Biol.* **17**, e3000284 (2019).
8. Amunts, K. *et al.* BigBrain: An Ultrahigh-Resolution 3D Human Brain Model. *Science (80-.).* **340**, 1472–1475 (2013).
9. Li, M. *et al.* Integrative functional genomic analysis of human brain development and neuropsychiatric risks. *Science (80-.).* **362**, eaat7615 (2018).
10. Mori, S., Crain, B. J., Chacko, V. P. & Van Zijl, P. C. M. Three-dimensional tracking of axonal projections in the brain by magnetic resonance imaging. *Ann. Neurol.* **45**, 265–269 (1999).
11. Conturo, T. E. *et al.* Tracking neuronal fiber pathways in the living human brain. *Proc. Natl. Acad. Sci. U. S. A.* **96**, 10422–10427 (1999).
12. Dyrby, T. B. *et al.* Validation of in vitro probabilistic tractography. *Neuroimage* **37**, 1267–1277 (2007).
13. Hagmann, P. *et al.* Mapping the structural core of human cerebral cortex. *PLoS Biol.* **6**, 1479–1493 (2008).
14. Ingalhalikar, M. *et al.* Sex differences in the structural connectome of the human brain. *Proc. Natl. Acad. Sci.* **111**, 823–828 (2014).
15. Sizemore, A. E. *et al.* Cliques and cavities in the human connectome. *J. Comput. Neurosci.* **44**, 115–145 (2018).
16. Yau, Y. *et al.* Network connectivity determines cortical thinning in early Parkinson's disease progression. *Nat. Commun.* **9**, 12 (2018).
17. Bernhardt, B. C. *et al.* Temporal lobe epilepsy: Hippocampal pathology modulates connectome topology and controllability. *Neurology* **92**, e2209–e2220 (2019).
18. van den Heuvel, M. P. & Sporns, O. A cross-disorder connectome landscape of brain dysconnectivity. *Nat. Rev. Neurosci.* **20**, 435–446 (2019).
19. Deco, G. *et al.* How local excitation-inhibition ratio impacts the whole brain dynamics. *J. Neurosci.* **34**, 7886–98 (2014).
20. Cabral, J., Hugues, E., Kringelbach, M. L. & Deco, G. Modeling the outcome of structural disconnection on resting-state functional connectivity. *Neuroimage* **62**, 1342–1353 (2012).
21. Mišić, B. *et al.* Network-Level Structure-Function Relationships in Human Neocortex. *Cereb.*

Cortex **26**, 3285–96 (2016).

22. Honey, C. J. *et al.* Predicting human resting-state functional connectivity from structural connectivity. *Proc. Natl. Acad. Sci. U. S. A.* **106**, 2035–40 (2009).
23. Betzel, R. F. *et al.* The community structure of functional brain networks exhibits scale-specific patterns of inter- and intra-subject variability. *Neuroimage* (2019). doi:10.1016/j.neuroimage.2019.07.003
24. Mollink, J. *et al.* The spatial correspondence and genetic influence of interhemispheric connectivity with white matter microstructure. *Nat. Neurosci.* **22**, 809–819 (2019).
25. Jones, D. K., Knösche, T. R. & Turner, R. White matter integrity, fiber count, and other fallacies: The do's and don'ts of diffusion MRI. *Neuroimage* **73**, 239–254 (2013).
26. Maier-Hein, K. H. *et al.* The challenge of mapping the human connectome based on diffusion tractography. *Nat. Commun.* **8**, 1349 (2017).
27. Schüz, A., Braitenberg, V. & Braitenberg, V. The Human Cortical White Matter: Quantitative Aspects of Cortico-Cortical Long-Range Connectivity. 389–398 (2002). doi:10.1201/9780203299296-24
28. Ecker, C. *et al.* Intrinsic gray-matter connectivity of the brain in adults with autism spectrum disorder. *Proc. Natl. Acad. Sci.* **110**, 13222–13227 (2013).
29. Hong, S.-J., Valk, S. L., Di Martino, A., Milham, M. P. & Bernhardt, B. C. Multidimensional Neuroanatomical Subtyping of Autism Spectrum Disorder. *Cereb. Cortex* 1–11 (2017). doi:10.1093/cercor/bhx229
30. Scannell, J. W., Blakemore, C. & Young, M. P. Analysis of connectivity in the cat cerebral cortex. *J. Neurosci.* **15**, 1463–83 (1995).
31. Barbas, H. & Rempel-Clower, N. Cortical structure predicts the pattern of corticocortical connections. *Cereb. Cortex* **7**, 635–646 (1997).
32. Beul, S. F., Barbas, H. & Hilgetag, C. C. A Predictive Structural Model of the Primate Connectome. *Sci. Rep.* **7**, (2017).
33. Beul, S. F., Grant, S. & Hilgetag, C. C. A predictive model of the cat cortical connectome based on cytoarchitecture and distance. *Brain Struct. Funct.* **220**, 3167–3184 (2015).
34. Hilgetag, C. C. & Grant, S. Cytoarchitectural differences are a key determinant of laminar projection origins in the visual cortex. *Neuroimage* **51**, 1006–1017 (2010).
35. García-Cabezas, M. Á., Zikopoulos, B. & Barbas, H. The Structural Model: a theory linking connections, plasticity, pathology, development and evolution of the cerebral cortex. *Brain Struct. Funct.* 1–24 (2019). doi:10.1007/s00429-019-01841-9
36. Mesulam, M.-M. From sensation to cognition. *Brain* **121**, 1013–1052 (1998).
37. Margulies, D. S. *et al.* Situating the default-mode network along a principal gradient of macroscale cortical organization. *Proc. Natl. Acad. Sci.* **113**, 12574–12579 (2016).
38. Van Essen, D. C. *et al.* The WU-Minn Human Connectome Project: An overview. *Neuroimage* **80**, 62–79 (2013).
39. Coifman, R. R. & Lafon, S. Diffusion maps. *Appl. Comput. Harmon. Anal.* **21**, 5–30 (2006).
40. Bernhardt, B. C. *et al.* Preferential susceptibility of limbic cortices to microstructural damage in temporal lobe epilepsy: A quantitative T1 mapping study. *Neuroimage* **182**, 294–303 (2018).
41. Turner, R. Myelin and modeling: Bootstrapping cortical microcircuits. *Frontiers in Neural Circuits* **13**, (2019).

42. Marques, J. P. *et al.* MP2RAGE, a self bias-field corrected sequence for improved segmentation and T1-mapping at high field. *Neuroimage* **49**, 1271–1281 (2010).

43. Bock, N. A. *et al.* Optimizing T1-weighted imaging of cortical myelin content at 3.0T. *Neuroimage* **65**, 1–12 (2013).

44. Wang, D. *et al.* Comprehensive functional genomic resource and integrative model for the human brain. *Science* **362**, eaat8464 (2018).

45. Sanides, F. *Die Architektonik des menschlichen Stirnhirns zugleich eine Darstellung der Prinzipien seiner Gestaltung als Spiegel der stammgeschichtlichen Differenzierung der Grosshirnrinde.* 201 (Springer, 1962).

46. Vogt, C. & Vogt, O. Allgemeinere Ergebnisse unserer Hirnforschung. *J. für Psychol. und Neurol.* **25**, 279–461 (1919).

47. York, E. M., Bernier, L. P. & MacVicar, B. A. Microglial modulation of neuronal activity in the healthy brain. *Dev. Neurobiol.* **78**, 593–603 (2018).

48. Halassa, M. M. & Haydon, P. G. Integrated Brain Circuits: Astrocytic Networks Modulate Neuronal Activity and Behavior. *Annu. Rev. Physiol.* **72**, 335–355 (2010).

49. Yeo, B. T. T. *et al.* The organization of the human cerebral cortex estimated by intrinsic functional connectivity. *J. Neurophysiol.* **106**, 1125–1165 (2011).

50. Felleman, D. J. & Van Essen, D. C. Distributed hierarchical processing in the primate cerebral cortex. *Cereb. Cortex* **1**, 1–47 (1991).

51. Nolte, G. *et al.* Robustly estimating the flow direction of information in complex physical systems. *Phys. Rev. Lett.* **100**, (2008).

52. Michalareas, G. *et al.* Alpha-Beta and Gamma Rhythms Subserve Feedback and Feedforward Influences among Human Visual Cortical Areas Article Alpha-Beta and Gamma Rhythms Subserve Feedback and Feedforward Influences among Human Visual Cortical Areas. *Neuron* **89**, 384–397 (2016).

53. Gallivan, J. P., Chapman, C. S., Gale, D. J., Flanagan, J. R. & Culham, J. C. Selective Modulation of Early Visual Cortical Activity by Movement Intention. *Cereb. Cortex* **29**, 4662–4678 (2019).

54. Gutteling, T. P. *et al.* Action preparation shapes processing in early visual cortex. *J. Neurosci.* **35**, 6472–6480 (2015).

55. Amiri, A. *et al.* Transcriptome and epigenome landscape of human cortical development modeled in organoids. *Science (80-.).* **362**, (2018).

56. Coifman, R. R. *et al.* Geometric diffusions as a tool for harmonic analysis and structure definition of data: Multiscale methods. *Proc. Natl. Acad. Sci.* **102**, 7432–7437 (2005).

57. Huntenburg, J. M. *et al.* A Systematic Relationship Between Functional Connectivity and Intracortical Myelin in the Human Cerebral Cortex. *Cereb. Cortex* **27**, 981–997 (2017).

58. Haak, K. V., Marquand, A. F. & Beckmann, C. F. Connectopic mapping with resting-state fMRI. *NeuroImage* **170**, 83–94 (2018).

59. Badre, D. & D'Esposito, M. Is the rostro-caudal axis of the frontal lobe hierarchical? *Nature Reviews Neuroscience* **10**, 659–669 (2009).

60. Borghesani, V. *et al.* Word meaning in the ventral visual path: a perceptual to conceptual gradient of semantic coding. *Neuroimage* **143**, 128–140 (2016).

61. Goodale, M. A. & Milner, A. D. Separate visual pathways for perception and action. *Trends Neurosci.* **15**, 20–25 (1992).

62. Braga, R. M., Hellyer, P. J., Wise, R. J. S. & Leech, R. Auditory and visual connectivity gradients in frontoparietal cortex. *Hum. Brain Mapp.* **38**, 255–270 (2017).

63. Passingham, R. E., Stephan, K. E. & Kötter, R. The anatomical basis of functional localization in the cortex. *Nat. Rev. Neurosci.* **3**, 606–616 (2002).

64. Nachev, P., Kennard, C. & Husain, M. Functional role of the supplementary and pre-supplementary motor areas. *Nature Reviews Neuroscience* **9**, 856–869 (2008).

65. Hill, J. *et al.* Similar patterns of cortical expansion during human development and evolution. *Proc. Natl. Acad. Sci. U. S. A.* **107**, 13135–40 (2010).

66. Wei, Y. *et al.* Genetic mapping and evolutionary analysis of human-expanded cognitive networks. *Nat. Commun.* **10**, 4839 (2019).

67. Xu, T. *et al.* Cross-species Functional Alignment Reveals Evolutionary Hierarchy Within the Connectome. *bioRxiv* 692616 (2019). doi:10.1101/692616

68. Ramon y Cajal, S. *Histology of the nervous system of man and vertebrates*. (Oxford University Press, 1995).

69. Braitenberg, V. & Schüz, A. Cyto- and Myeloarchitectonics: Two Aspects of the same Reality. in *Cortex: Statistics and Geometry of Neuronal Connectivity* 151–158 (Springer Berlin Heidelberg, 1998). doi:10.1007/978-3-662-03733-1_29

70. Douglas, R. J., Martin, K. A. C. & Whitteridge, D. A Canonical Microcircuit for Neocortex. *Neural Comput.* **1**, 480–488 (1989).

71. Buffalo, E. A., Fries, P., Landman, R., Buschman, T. J. & Desimone, R. Laminar differences in gamma and alpha coherence in the ventral stream. *Proc. Natl. Acad. Sci. U. S. A.* **108**, 11262–7 (2011).

72. Bosman, C. A. *et al.* Attentional stimulus selection through selective synchronization between monkey visual areas. *Neuron* **75**, 875–88 (2012).

73. Scheeringa, R. & Fries, P. Cortical layers, rhythms and BOLD signals. *Neuroimage* **197**, 689–698 (2019).

74. Markov, N. T. *et al.* Anatomy of hierarchy: Feedforward and feedback pathways in macaque visual cortex. *J. Comp. Neurol.* **522**, 225–259 (2014).

75. Wang, Z., Gerstein, M. & Snyder, M. RNA-Seq: A revolutionary tool for transcriptomics. *Nature Reviews Genetics* **10**, 57–63 (2009).

76. Vasile, F., Dossi, E. & Rouach, N. Human astrocytes: structure and functions in the healthy brain. *Brain Struct. Funct.* **222**, 2017–2029 (2017).

77. Bass, N. H., Hess, H. H., Pope, A. & Thalheimer, C. Quantitative cytoarchitectonic distribution of neurons, glia, and DNA in rat cerebral cortex. *J. Comp. Neurol.* **143**, 481–490 (1971).

78. Pelvig, D. P., Pakkenberg, H., Stark, A. K. & Pakkenberg, B. Neocortical glial cell numbers in human brains. *Neurobiol. Aging* **29**, 1754–1762 (2008).

79. Oikonomou, G. & Shaham, S. The Glia of Caenorhabditis elegans. *Glia* **59**, 1253–1263 (2011).

80. Oberheim, N. A. *et al.* Uniquely hominid features of adult human astrocytes. *J. Neurosci.* **29**, 3276–87 (2009).

81. Glomb, K., Ponce-Alvarez, A., Gilson, M., Ritter, P. & Deco, G. Resting state networks in empirical and simulated dynamic functional connectivity. *Neuroimage* **159**, 388–402 (2017).

82. Braga, R. M., Sharp, D. J., Leeson, C., Wise, R. J. S. & Leech, R. Echoes of the brain within default mode, association, and heteromodal cortices. *J. Neurosci.* **33**, 14031–9 (2013).

83. Braga, R. M. & Leech, R. Echoes of the Brain: Local-Scale Representation of Whole-Brain Functional Networks within Transmodal Cortex. *Neuroscientist* **21**, 540 (2015).

84. Leech, R., Braga, R. & Sharp, D. J. Echoes of the brain within the posterior cingulate cortex. *J. Neurosci.* **32**, 215–22 (2012).

85. Vázquez-Rodríguez, B. *et al.* Gradients of structure–function tethering across neocortex. *Proc. Natl. Acad. Sci.* 201903403 (2019). doi:10.1073/pnas.1903403116

86. Baum, G. L. *et al.* Development of structure–function coupling in human brain networks during youth. *Proc. Natl. Acad. Sci.* 201912034 (2019). doi:10.1073/pnas.1912034117

87. Preti, M. G. & Van De Ville, D. Decoupling of brain function from structure reveals regional behavioral specialization in humans. *Nat. Commun.* **10**, (2019).

88. Moraes Bastos, A. *et al.* Visual Areas Exert Feedforward and Feedback Influences through Distinct Frequency Channels Article Visual Areas Exert Feedforward and Feedback Influences through Distinct Frequency Channels. *Neuron* **85**, 390–401 (2015).

89. Michalareas, G. *et al.* Alpha-Beta and Gamma Rhythms Subserve Feedback and Feedforward Influences among Human Visual Cortical Areas. *Neuron* **89**, (2016).

90. Fries, P. Rhythms for Cognition: Communication through Coherence. *Neuron* **88**, 220–235 (2015).

91. Betzel, R. F. *et al.* Structural, geometric and genetic factors predict interregional brain connectivity patterns probed by electrocorticography. *Nat. Biomed. Eng.* (2019). doi:10.1038/s41551-019-0404-5

92. Vos de Wael, R. *et al.* BrainSpace: a toolbox for the analysis of macroscale gradients in neuroimaging and connectomics datasets. *bioRxiv* 761460 (2019). doi:10.1101/761460

93. Glasser, M. F. *et al.* The minimal preprocessing pipelines for the Human Connectome Project. *Neuroimage* **80**, 105–124 (2013).

94. Fischl, B., Sereno, M. I. & Dale, A. M. Cortical surface-based analysis. II: Inflation, flattening, and a surface-based coordinate system. *Neuroimage* **9**, 195–207 (1999).

95. Dale, A. M., Fischl, B. & Sereno, M. I. Cortical surface-based analysis. I. Segmentation and surface reconstruction. *Neuroimage* **9**, 179–194 (1999).

96. Fischl, B., Sereno, M. I., Tootell, R. B. & Dale, A. M. High-resolution intersubject averaging and a coordinate system for the cortical surface. *Hum. Brain Mapp.* **8**, 272–284 (1999).

97. Glasser, M. F. & Van Essen, D. C. Mapping human cortical areas in vivo based on myelin content as revealed by T1- and T2-weighted MRI. *J. Neurosci.* **31**, 11597–616 (2011).

98. Salimi-Khorshidi, G. *et al.* Automatic denoising of functional MRI data: Combining independent component analysis and hierarchical fusion of classifiers. *Neuroimage* **90**, 449–468 (2014).

99. Robinson, E. C. *et al.* Multimodal surface matching with higher-order smoothness constraints. *Neuroimage* **167**, 453–465 (2018).

100. Robinson, E. C. *et al.* MSM: A new flexible framework for multimodal surface matching. *Neuroimage* **100**, 414–426 (2014).

101. Desikan, R. S. *et al.* An automated labeling system for subdividing the human cerebral cortex on MRI scans into gyral based regions of interest. *Neuroimage* **31**, 968–980 (2006).

102. Larivière, S. *et al.* Functional Connectome Contractions in Temporal Lobe Epilepsy. *bioRxiv* 756494 (2019). doi:10.1101/756494

103. Wagstyl, K., Paquola, C., Bethlehem, R. & Huth, A. kwagstyl/surface_tools: Initial release of equivolumetric surfaces. (2018). doi:10.5281/ZENODO.1412054

104. Dhollander, T., Raffelt, D. & Connelly, A. Unsupervised 3-tissue response function estimation from single-shell or multi-shell diffusion MR data without a co-registered T1 image. in *ISMRM Workshop on Breaking the Barriers of Diffusion MRI* 5 (2016).

105. Jeurissen, B., Tournier, J.-D., Dhollander, T., Connelly, A. & Sijbers, J. Multi-tissue constrained spherical deconvolution for improved analysis of multi-shell diffusion MRI data. *Neuroimage* **103**, 411–426 (2014).

106. Tournier, J. D., Calamante, F. & Connelly, A. Robust determination of the fibre orientation distribution in diffusion MRI: Non-negativity constrained super-resolved spherical deconvolution. *Neuroimage* **35**, 1459–1472 (2007).

107. Smith, R. E., Tournier, J. D., Calamante, F. & Connelly, A. SIFT2: Enabling dense quantitative assessment of brain white matter connectivity using streamlines tractography. *Neuroimage* **119**, 338–351 (2015).

108. Betzel, R. F., Griffa, A., Hagmann, P. & Misic, B. Distance-dependent consistency thresholds for generating group-representative structural brain networks. *Netw. Neurosci.* 412346 (2018). doi:10.1101/412346

109. Wang, B. *et al.* Similarity network fusion for aggregating data types on a genomic scale. *Nat. Methods* **11**, 333–337 (2014).

110. Von Luxburg, U. A tutorial on spectral clustering. *Stat. Comput.* **17**, 395–416 (2007).

111. Tenenbaum, J. B., De Silva, V. & Langford, J. C. A global geometric framework for nonlinear dimensionality reduction. *Science (80-.).* **290**, 2319–23 (2000).

112. Vos de Wael, R. *et al.* Anatomical and microstructural determinants of hippocampal subfield functional connectome embedding. *Proc. Natl. Acad. Sci. U. S. A.* **115**, 10154–10159 (2018).

113. Wagstyl, K. *et al.* Mapping Cortical Laminar Structure in the 3D BigBrain. *Cereb. Cortex* **28**, 2551–2562 (2018).

114. Lake, B. B. *et al.* Integrative single-cell analysis of transcriptional and epigenetic states in the human adult brain. *Nat. Biotechnol.* **36**, 70 (2018).

115. Seidlitz, J. *et al.* Transcriptomic and Cellular Decoding of Regional Brain Vulnerability to Neurodevelopmental Disorders. *bioRxiv* 573279 (2019). doi:10.1101/573279

116. Wagner, H. H. & Dray, S. Generating spatially constrained null models for irregularly spaced data using Moran spectral randomization methods. *Methods Ecol. Evol.* **6**, 1169–1178 (2015).

117. Alexander-Bloch, A. F. *et al.* On testing for spatial correspondence between maps of human brain structure and function. *Neuroimage* **178**, 540–551 (2018).

118. Benjamini, Y. & Hochberg, Y. Controlling the False Discovery Rate: A Practical and Powerful Approach to Multiple Testing. *J. R. Stat. Soc. Ser. B* **57**, 289–300 (1995).

119. Haast, R. A. M., Ivanov, D., Formisano, E. & Uludağ, K. Reproducibility and Reliability of Quantitative and Weighted T1 and T2∗ Mapping for Myelin-Based Cortical Parcellation at 7 Tesla. *Front. Neuroanat.* **10**, 112 (2016).

120. Griffanti, L. *et al.* ICA-based artefact removal and accelerated fMRI acquisition for improved resting state network imaging. *Neuroimage* **95**, 232–247 (2014).

121. Jurysta, F. *et al.* A study of the dynamic interactions between sleep EEG and heart rate variability in healthy young men. *Clin. Neurophysiol.* **114**, 2146–2155 (2003).

122. Carter, G. C., Knapp, C. H. & Nuttall, A. H. Estimation of the Magnitude-Squared Coherence Function Via Overlapped Fast Fourier Transform Processing. *IEEE Trans. Audio Electroacoust.* **21**, 337–344 (1973).

123. Lancichinetti, A. & Fortunato, S. Consensus clustering in complex networks. *Sci. Rep.* **2**, (2012).

124. Oostenveld, R., Fries, P., Maris, E. & Schoffelen, J.-M. FieldTrip: Open source software for advanced analysis of MEG, EEG, and invasive electrophysiological data. *Comput. Intell. Neurosci.* **2011**, 156869 (2011).

125. The MathWorks, I. MATLAB and Statistics Toolbox Release. (2017).

126. Mesulam, M.-M. Behavioral neuroanatomy: Largescale networks, association cortex, frontal syndromes, the limbic system, and hemispheric specialization. in *Principles of Behavioral and Cognitive Neurology* 1–120 (2000).

127. Adler, S. *et al.* Topographic principles of cortical fluid-attenuated inversion recovery signal in temporal lobe epilepsy. *Epilepsia* **59**, 627–635 (2018).

SUPPLEMENTARY MATERIAL

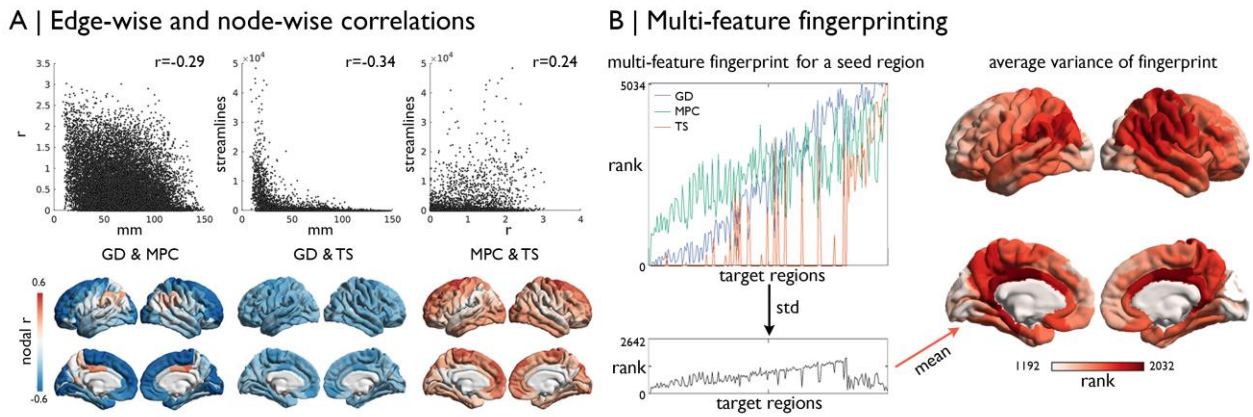

Figure S1: (A) Scatterplots depict the global correlation between the different cortical wiring features *i.e.*, geodesic distance (GD), microstructure profile covariance (MPC), and diffusion-based tract strength (TS). Average r values for each node are projected below on the cortical surface. **(B)** Fingerprinting involved combining all three wiring features of one region. The standard deviation across the three features was estimated for each edge, then the average was taken for each node as a measure of feature variance of the fingerprint.

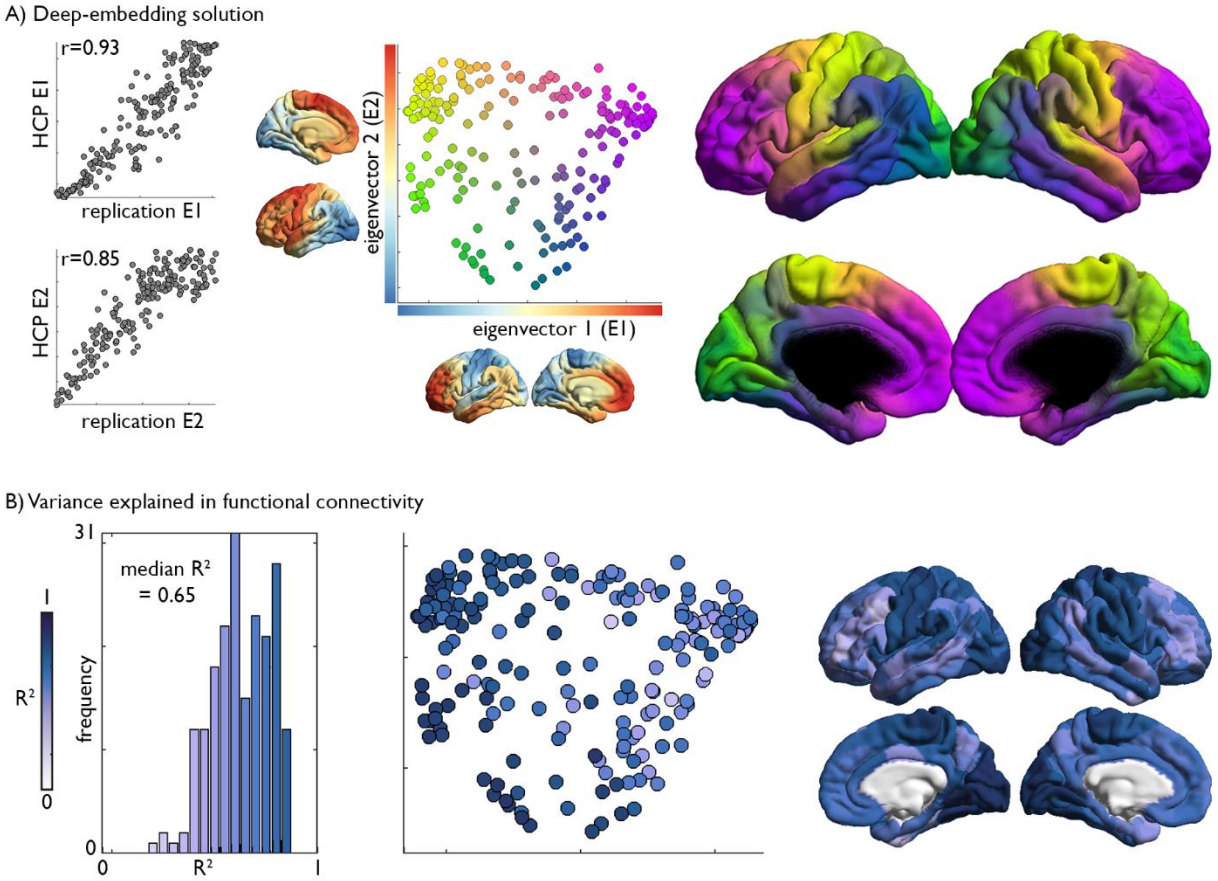

Figure S2: Independent replication of the structural manifold. The structural manifold was regenerated using an independent *Replication* dataset of 40 healthy adults scanned at our imaging centre. Imaging parameters were similar to the original cohort, albeit using quantitative T1 relaxometry as a marker of cortical microstructure rather than HCP's T1w/T2w ratio mapping. **(A)** Scatterplots show marked correspondence between the original HCP *Discovery* sample eigenvectors and those from the *Replication* dataset, with Spearman correlations shown. **(B)** Using boosting regression, we similarly found that high, but regionally variable, variance in the group-average functional connectivity could be explained by the structural manifold in the *Replication* dataset.

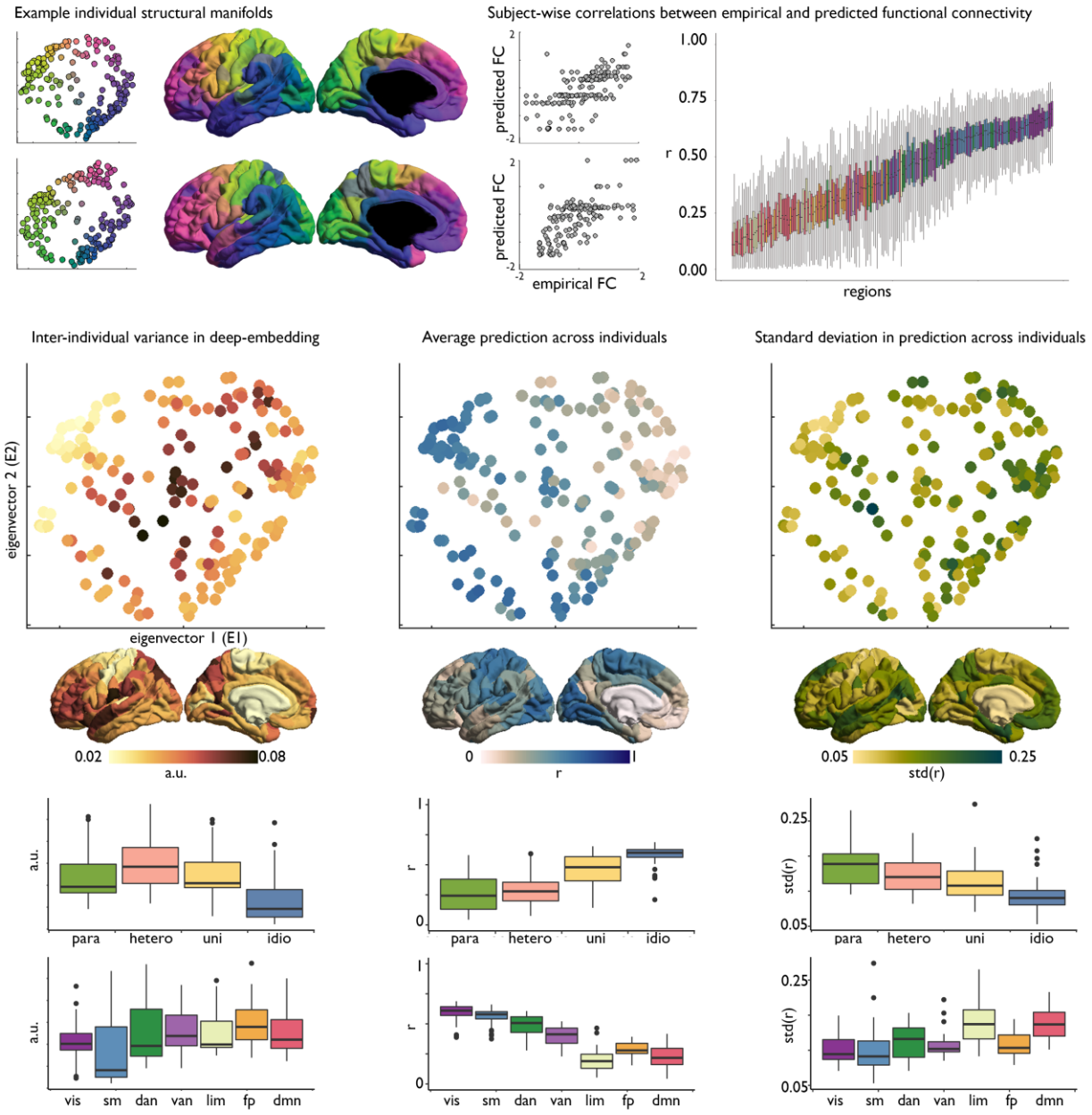

Figure S3: Individual variation in the structural manifold and prediction of rs-fMRI connectivity. Individual variation was calculated as the Euclidean distance between the node's position in the subject vs group-average structural manifold, where the position is synonymous with the values on the first two eigenvectors following Procrustes alignment. Inter-individual variance was taken as the average across all subjects and provided as arbitrary units (a.u.). We also calculated the mean and SD in the correlation between predicted and empirical functional connectivity for each node across subjects. Node-wise values are presented in the structural manifold, on the cortical surface and stratified by level of laminar differentiation [7,126] and functional network [49].

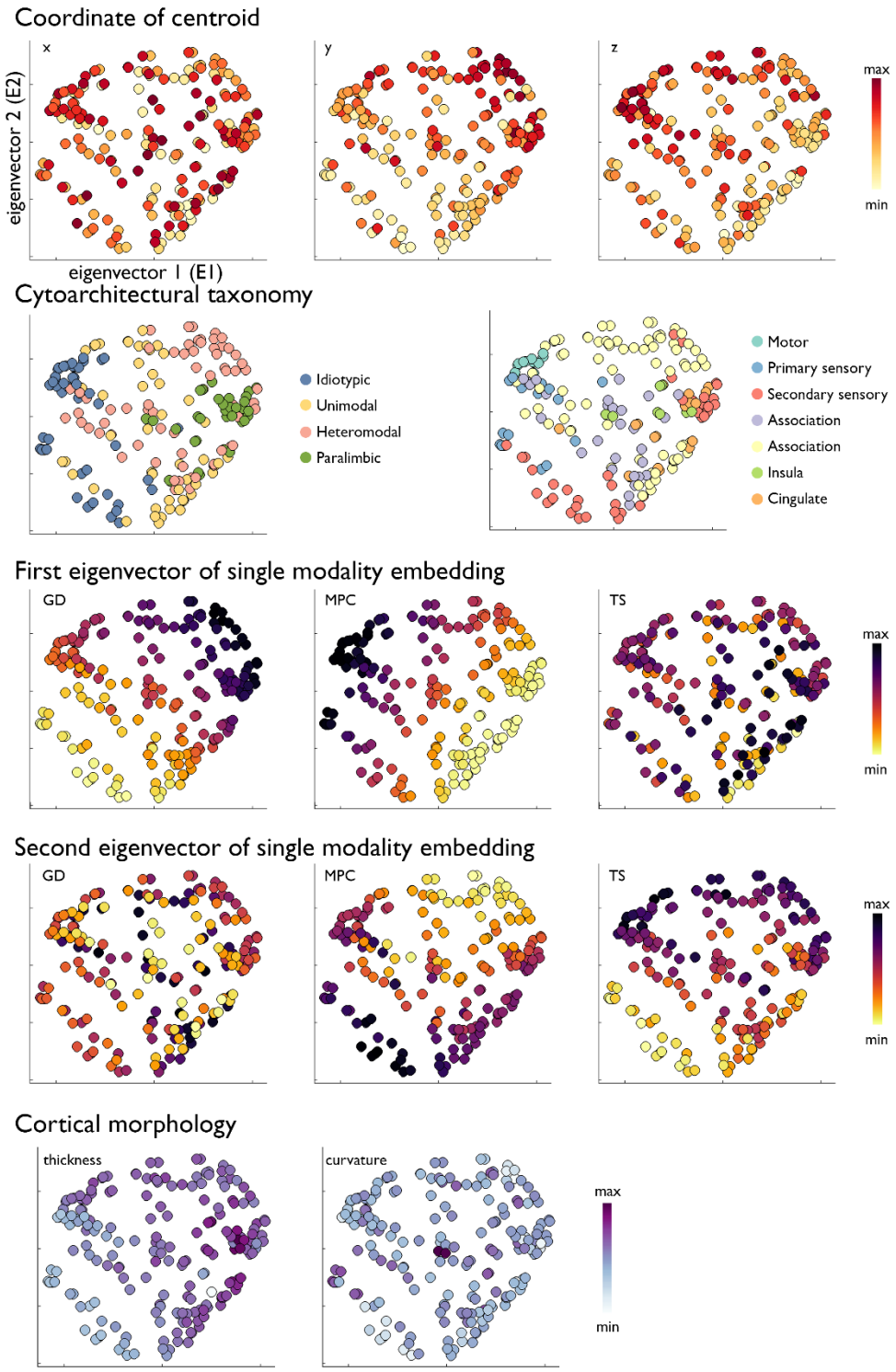

Figure S4: Patterns in structural manifold. (Top) Centroid coordinate of each parcel. x=left-right, y=posterior-anterior, z=inferior-superior. **(2nd row)** Node-wise assignment to level of laminar differentiation [7,126] and class of cytoarchitectural complexity [127]. **(3rd & 4th row)** Principles gradients from single modalities. **(5th row)** Group-average cortical thickness and curvature measures in the manifold.

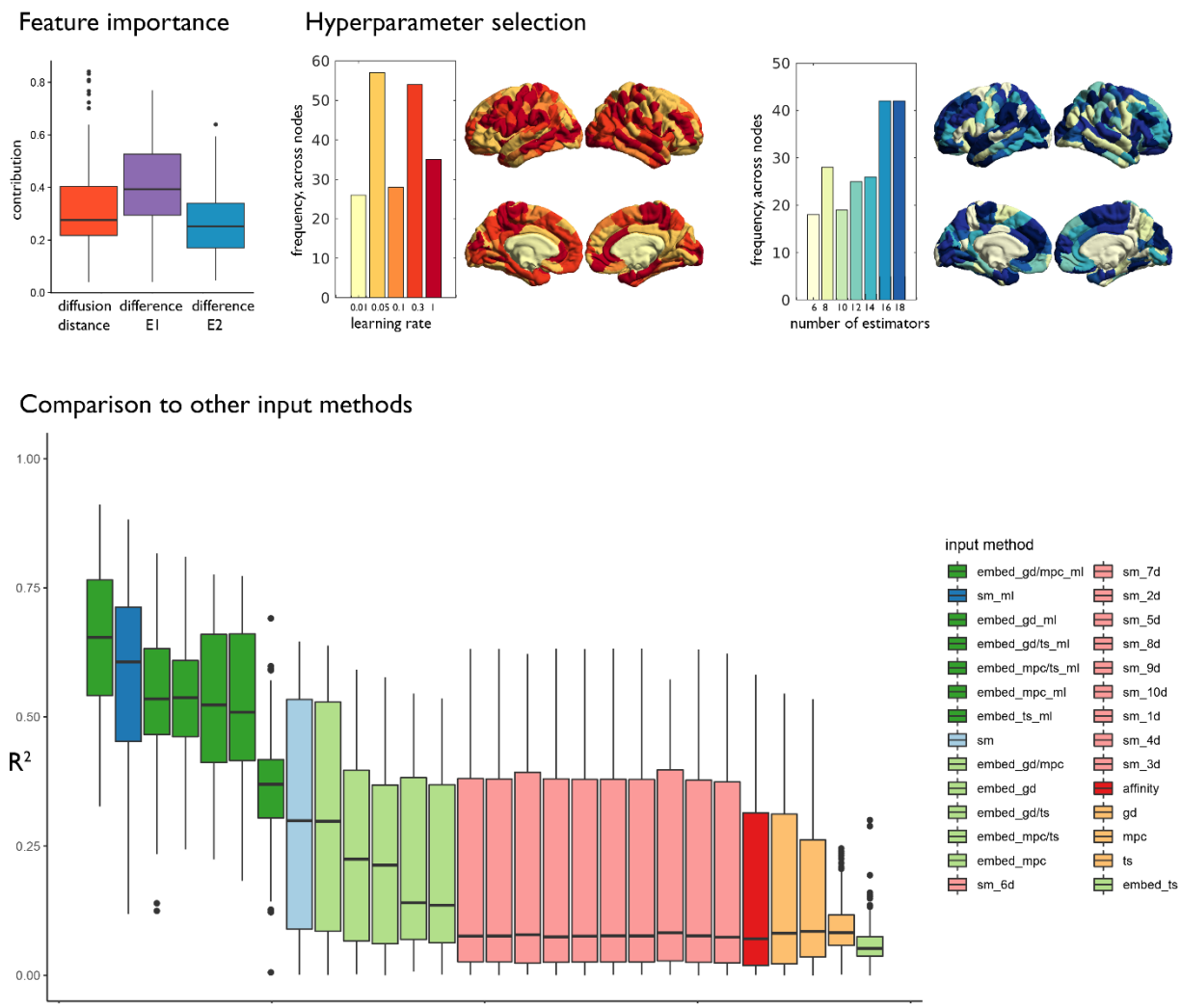

Figure S5: Modelling rs-fMRI connectivity from the structural manifold. As the procedure was repeated for each node independently, we here present the range of feature importance, selected hyperparameters, and adjusted R^2 values across nodes. For model comparison, rs-fMRI connectivity was modelled with linear regression unless machine learning is signified by "ml". "sm" represents structural manifold, that is the model with GD, MPC, and TS. The "1d-10d" approaches were based on 1-10 eigenvectors from the structural manifold solution and used the Euclidean distance in the multi-dimensional approach to predict functional connectivity.

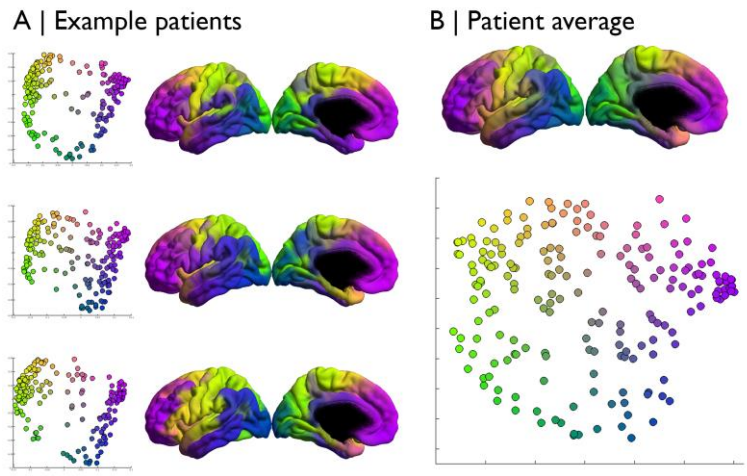

Figure S6: Patient structural manifolds. **(A)** Structural manifolds were generated for each of the ten patients. **(B)** The average structural manifold across the patients was highly similar to the healthy template (correlations between eigenvectors 1/2: r=0.83/0.82).

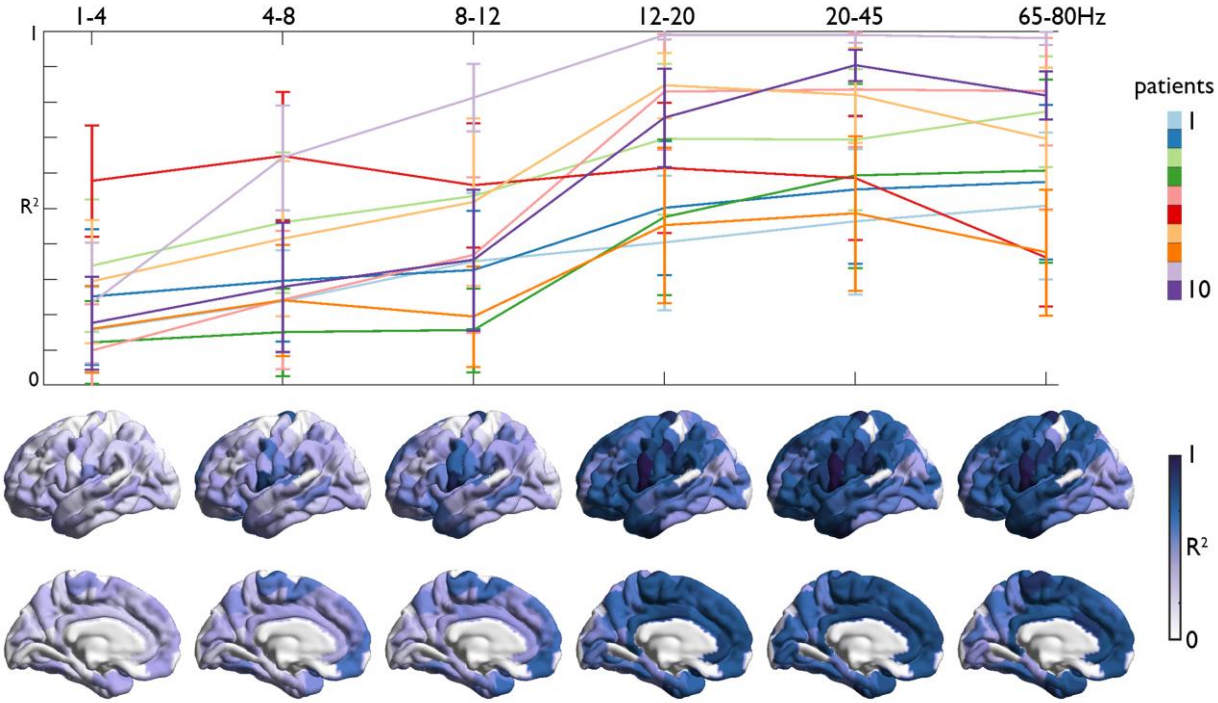

Figure S7: Variance explained in frequency binned undirected coherence. (Top) Mean±SD in R^2 for each patient. **(B)** Mean R^2 for each parcel, mirrored across the hemispheres. No electrodes were placed in six parcels and are seen as white in all cortical projections; medial orbitofrontal cortex, superior precentral cortex, frontal pole, occipital pole, lingual gyrus and posterior superior temporal gyrus.

Table S1: Statistical relationships between cell type specific gene expression and structural manifold.

	Regional expression modelled by structural manifold eigenvectors 1 & 2[1]		Spearman correlation between co-expression and manifold distance			
			Full correlation		Corrected for geodesic distance	
Cell type	r	p[2]	r	p	r	p
Astrocyte	0.91	0.0019	-0.74	<0.001	-0.48	0.0007
Endothelial cells	0.81	0.2817	-0.55	<0.001	-0.28	0.0017
Microglia	0.76	0.0368	-0.75	<0.001	-0.53	<0.001
Neurons – excitatory	0	0.1271	-0.68	<0.001	-0.42	<0.001
Neurons – inhibitory	0.46	0.0404	-0.68	<0.001	-0.41	0.0001
OPCs	0.89	0.0273	-0.65	<0.001	-0.34	0.0002
Oligodendrocytes	0	0.3601	-0.52	<0.001	-0.33	0.0002
Pericytes	0.35	0.2534	-0.64	<0.001	-0.33	0.0002

[1] Expression ~ $1+ \beta_1 \text{eigenvector1} + \beta_2 \text{eigenvector2} + \varepsilon$

[2] Comparison to null model with 10000 permutations of spatial maps with matched spatial autocorrelation [116]

Table S2: Variance explained in externopyramidisation with alternative input measures

	Adjusted R^2
GD only	0.50975
MPC only	0.49381
TS only	0.62106
GD + MPC	0.64716
GD + TS	0.52581
MPC + TS	0.54945
GD, MPC + TS	**0.65076**

Table S3: Statistical outcomes of linear mixed effect model of phase slope index between structural manifold clusters. Positive t-statistics represent the row-cluster driving oscillations to the column-cluster, whereas negative t-statistics represent the row-cluster receiving oscillations from the column-cluster. Phase slope index was operationalised within six standard frequency bands: delta (1:4), theta (4:8), alpha (8:12), low beta (12:20), high beta (20:45) and gamma (65:80).

Frequency band, Hz		t-statistic (whole cohort ± SD across leave-one-out)					
	cluster	1	2	3	4	5	6
1:4	1	-0.03±0.02	-4.3±0.77	-4.53±1.45	0.45±1.21	0.48±1.87	-0.49±0.84
	2	4.32±0.77	-0.02±0.01	-0.79±1.9	1.45±1.16	7.45±1.74	6.27±2.06
	3	4.64±1.44	0.81±1.87	-0.03±0.01	1.66±1.86	3.76±0.77	5.41±1.02
	4	-0.46±1.21	-1.37±1.16	-1.52±1.87	-0.03±0.01	-0.32±1.45	0.55±1.22
	5	-0.44±1.87	-7.42±1.73	-3.73±0.78	0.39±1.45	0.07±0.01	1.29±1.17
	6	0.55±0.85	-6.19±2.05	-5.29±1.03	-0.53±1.22	-1.22±1.17	-0.03±0.01
4:8	1	-0.02±0.02	-4.67±2.71	-6.55±0.52	1.38±1.44	-1.89±1.8	2.58±1.54
	2	4.68±2.72	-0.02±0.01	-2.29±1.77	3.42±1.56	-0.01±1.95	4.37±2.11
	3	6.64±0.53	2.31±1.75	-0.02±0.01	3.56±1.05	3.35±1.28	8.36±1.34
	4	-1.38±1.44	-3.35±1.56	-3.45±1.06	-0.03±0.01	-2.41±1.37	1.99±1.4
	5	1.93±1.8	0.03±1.95	-3.32±1.28	2.46±1.37	0.06±0.01	-0.88±0.74
	6	-2.53±1.54	-4.3±2.1	-8.25±1.35	-1.97±1.4	0.93±0.74	-0.02±0.01
8:12	1	-0.02±0.02	-3.33±1.81	-5.15±0.46	1.44±2.13	-1.61±0.81	-1.79±0.9
	2	3.35±1.81	-0.02±0.01	-4.67±1.3	3±1.16	5.75±2.44	1.95±0.78
	3	5.23±0.46	4.69±1.29	-0.02±0.01	8.65±1.67	8.56±0.62	5.07±0.8
	4	-1.44±2.13	-2.94±1.16	-8.55±1.68	-0.02±0.01	1.45±1.06	-1.06±0.51
	5	1.65±0.82	-5.73±2.42	-8.54±0.62	-1.41±1.05	0.05±0.01	-2.84±1.02
	6	1.84±0.91	-1.9±0.77	-4.98±0.81	1.08±0.51	2.89±1.02	-0.02±0.01
12:20	1	0.02±0.01	1.39±0.97	2.18±1.53	-0.23±0.77	4.6±1.81	5.73±1.49
	2	-1.4±0.97	0.01±0.01	5.72±1.46	0.02±2.35	1.16±1.5	4.7±1.37
	3	-2.26±1.52	-5.73±1.46	0.02±0.01	0±2.09	4.98±0.84	0.38±2.07
	4	0.23±0.76	-0.08±2.34	-0.09±2.08	0.02±0	-1.58±2.27	3.79±0.97
	5	-4.64±1.82	-1.17±1.5	-5±0.84	1.53±2.27	-0.05±0.01	-1.67±1.7
	6	-5.78±1.49	-4.75±1.37	-0.46±2.07	-3.81±0.97	1.63±1.7	0.02±0.01
20:45	1	-0.01±0.01	-0.78±0.56	-2.7±0.53	2.97±0.61	-1.16±1.07	1.51±0.73
	2	0.79±0.56	0±0	-3.86±1.05	4.82±0.63	2.27±1.04	0.17±0.87
	3	2.72±0.52	3.87±1.04	-0.01±0	6.17±1.16	1.34±0.57	7.65±1.03
	4	-2.97±0.61	-4.8±0.63	-6.14±1.17	-0.01±0	-1.61±0.71	-3.86±0.59
	5	1.17±1.07	-2.26±1.02	-1.33±0.57	1.62±0.71	0.01±0.01	2.58±0.69
	6	-1.5±0.72	-0.16±0.87	-7.62±1.04	3.86±0.59	-2.57±0.69	-0.01±0
65:80	1	-0.02±0.01	-0.81±0.61	3.02±0.53	-2.82±0.56	-6.04±0.96	-2.69±1.2
	2	0.83±0.61	-0.02±0.01	1.06±0.73	0.47±0.82	-2.66±0.75	-3.42±1.1
	3	-2.92±0.53	-1.03±0.73	-0.02±0.01	-2.74±0.82	-0.52±1.05	-3.06±0.84
	4	2.81±0.56	-0.4±0.82	2.85±0.81	-0.02±0	-4.96±0.73	-2.5±0.63
	5	6.08±0.97	2.68±0.75	0.55±1.05	5.01±0.73	0.05±0.01	-2.55±0.6
	6	2.74±1.2	3.49±1.1	3.14±0.85	2.52±0.63	2.61±0.6	-0.02±0.01